SUPPRESSION POOL DYNAMICS

Quarterly Progress Report
July 1, 1976 - September 30, 1976

POOR
ORIGINAL

University of California at Los Angeles
for
U. S. Nuclear Regulatory Commission

7909120462

731 065

731 066

SUPPRESSION POOL DYNAMICS

Quarterly Progress Report
July 1, 1976 - September 30, 1976

I. Catton
C. K. Chan
V. K. Dhir
C. Y. Liu

731 067

731 068

ABSTRACT

Transient air-water tests were performed as part of the laboratory
scale experiments project to investigate hydraulic response in a BWR Pressure
Suppression Containment at the onset of a LOCA. These tests were performed
in a cylindrical plexiglass test chamber. Air was injected downward through
pipes of different diameters placed in the middle of the test chamber con-
taining water at room temperature. Tests were performed to investigate the
effects of submergence depth and dry well pressure on the vent clearing
phenomena. Data were also obtained for the pool swell height under the
influence of a steady submerged air flow stream, although it is directly
not applicable to the BWR LOCA condition.

In parallel to the experimental efforts, scaling laws were established
for vent clearing, bubble growth, bubble motion and pool surface swelling.
The basic governing parameters for vent clearing are found to be the Froude
number and the Euler number while for other cases, in addition to the Froude
and the Euler numbers, the Mach number is found to be important.

Test data show that the vent clearing process can be approximately
modelled by considering the motion of a slug of water under the influence
of constant upstream pressure. However, the no slip boundary at the tube
wall and Taylor instability leads to some liquid film holdup during the time
it takes for the main water slug to clear the tube. Subsequently, Kelvin
Helmoltz instabilities break up the gas liquid interface forming a two-phase
region behind the slug. Comparisons with theoretical results reveal the
significance of this two-phase region on the prediction of vent clearing
time. In the quasi-steady air injection experiments, the swelling height
is found to correlate well with a modified Froude number.

731 069

iii

LIST OF SYMBOLS

A	tube area or cross-section
a	major radii
b	minor radii
c	minor radii
C_v	specific heat at constant volume
C_p	specific heat at constant pressure
D	test chamber diameter
d	vent tube diameter
e	eccentricity
Fr	Froude number
f_m	Fanno friction factor
g	gravitational constant
h	maximum swelling height
L	submergence depth
m	total mass
$\dot{m}$	mass influx
m_{ao}	apparent mass
ΔP	pressure difference
P_2	pressure in water pool
P_c	characteristic pressure
P_D	dry well pressure
P_s	wet well pressure
R	gas constant
r	radial co-ordinate or bubble radius
T	temperature

t	time
t_c	characteristic time
U	characteristic velocity
u	velocity
V	volume
v	velocity
x	interfacial location
z	axial co-ordinate
ρ	density
γ	isentropic gas constant
β	virtual mass parameter

Subscript

a	air
b	bubble
c	characteristic
m	model
p	prototype, suppression pool
s	stagnation properties
w	water

Superscript

$*$	Non-dimensional variable

LIST OF FIGURES

Page

731 073

LIST OF TABLES

731 074

TABLE OF CONTENTS

731 075

1.1 General

Transient air-water tests were performed in a transparent vessel to investigate vent clearing and pool swell phenomena that are expected to be experienced in a BWR Pressure Suppression Pool at the onset of a Loss of Coolant Accident (LOCA). These tests are part of an experimental program conducted at UCLA to investigate related thermal hydraulic phenomena that might affect the structural integrity of the Pressure Suppression Pool in the event of a LOCA. The program emphasizes fundamental understanding of the physical processes that ontrol the BWR system behavior. The results from this program are part of .ie Nuclear Regulatory Commission (NRC) data base which is used for evaluating the adequacy and improving the predictive capability of analytical models developed to predict system response during a LOCA. In addition, the results of these small scale tests are also valuable for comparison with data from similar investigations in larger geometries to aid in evaluating the effects of physical scale.

The experimental program is made up of three different test programs which will be coordinated to provide a basic understanding of the thermal hydraulic phenomena experienced in a Pressure Suppression Pool during LOCA transient. The air-water tests, which are reported herein, were conducted to investigate vent clearing and pool swelling phenomena in a laboratory-scale test facility, and to determine whether these phenomena have been adequately described in terms of current vent clearing models. These tests constitute the first phase of the air-water test program. Subsequent tests of the program would involve hydrodynamical force measurement and solid wall effects on the fluid transient.

The steam-water tests will be the second test program conducted to investigate steady state and transient submerged steam flow in a water medium where

condensation modes could produce undesirable forces. The concluding test program, the air-steam tests, will be conducted to investigate effects of non-condensibles on steam flow transients.

In addition to the three test programs, extensive efforts were spent in establishing the appropriate scaling laws for vent clearing, bubble growth, bubble motion and pool surface swelling for an injection. The results of this investigation are also included in this report. Future efforts in scaling would be for pure steam condensation and also for steam condensation in the presence of air.

1.2 Program Objectives

Current BWR Mark I containment designs utilize a water pool for pressure suppression, see Figure 1-1. One of the characteristics of a BWR suppression pool is the compartmental arrangement within the containment boundaries. In the event of a loss of coolant accident, the steam from the primary coolant pressurizes the dry well. This pressure rise pushes the water initially standing in the vent pipe into the suppression pool. The vent clearing is followed by the air-steam mixture. The steam condenses in the pool leaving the air which is initially at drywell pressure to expand and to rise up in the pool. The air pressure causes a downward load on the torus and the air expansion displaces the free surface upward. The accelerating free surface would cause an impact load on the structure in its path. These structures, which include the internal ring header and the support columns, are critical to the pressure suppression function. The continued inflow of air leads to bubble breakup creating a two phase froth of air and water. The air is finally released into the wet well atmosphere which is then pressurized. The fall back of the free surface causes more wavy motion. There is specu- lation that the vent opening might be uncovered. During the later stages of the accident, when the steam flow rate is low, water can re-enter the vent pipe when the steam

2
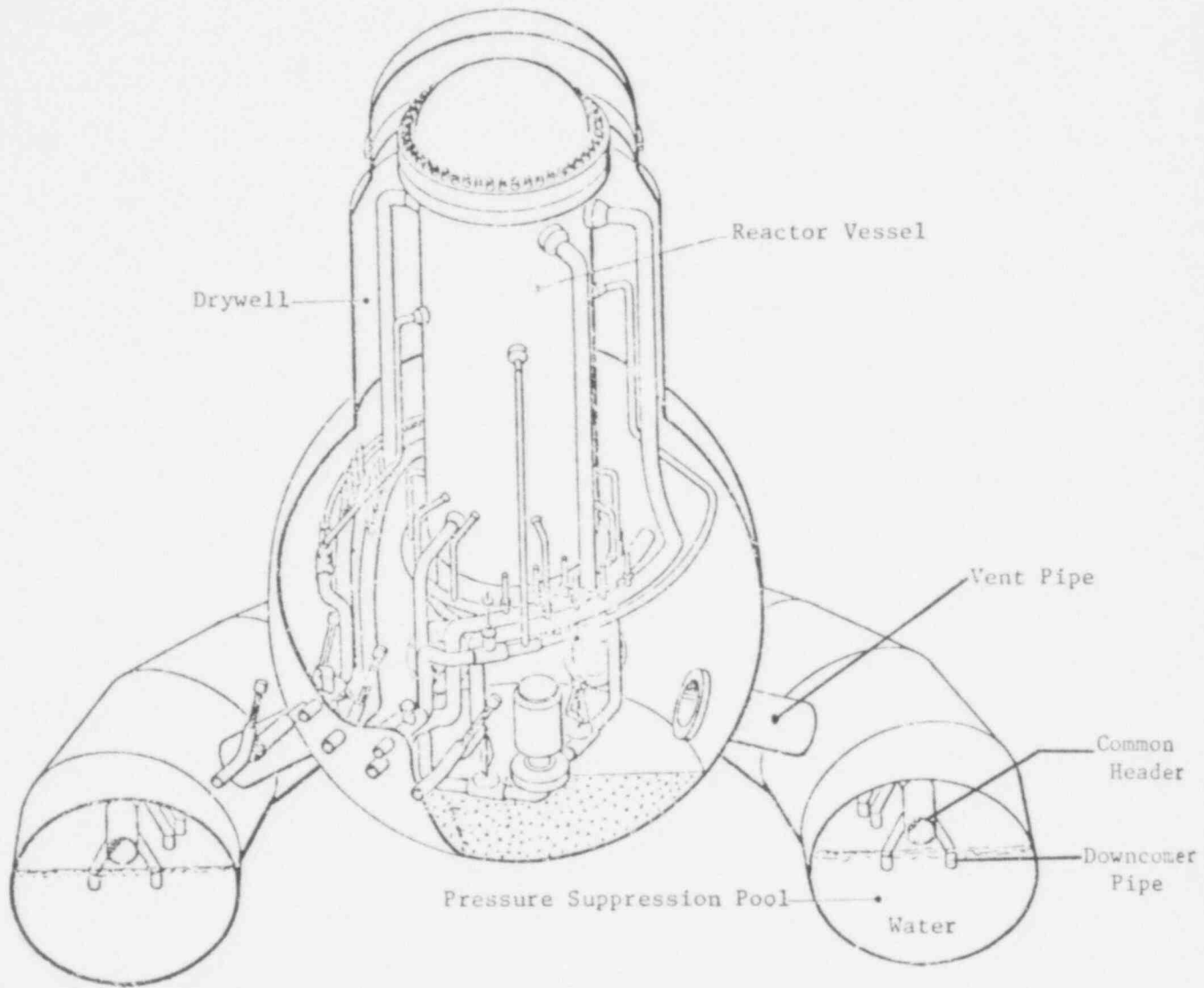
731 077

Figure 1.1. BWR Mark-I Primary Containment

The labels on the figure read:
- Reactor Vessel
- Drywell
- Vent Pipe
- Common Header
- Downcomer Pipe
- Pressure Suppression Pool
- Water

731 078

bubble collapses. A cyclic phenomena or chugging occurs that leads to oscillatory loading of the piping and surrounding structures. In Mark I design, a pressure chugging force would be applied to the downcomer pipe. Axisymmetric steam condensation at the exit would also impose a lateral loading on the downcomer.

The transient air and steam injection test program was initiated at UCLA on the 1st of July. The basic purpose of the experimental program is to develop an understanding of the interacting thermal and hydraulic phenomena occurring during injection of steam air mixtures in subcooled water. The specific objectives of the test programs at UCLA are to:

(i) investigate the transient flow phenomenon that occur in a tube similar to the vent clearing phase and determine whether the commonly used vent clearing model [1] describe adequately the phenomena,

(ii) investigate the transient pool surface motion,

(iii) investigate the dynamical forces during the entire transient,

(iv) investigate the transient steam flow in subcooled water,

(v) investigate the effect of the presence of air in steam condensation

(vi) establish appropriate scaling laws for the air and the steam transients, and

(vii) investigate experimental error magnification effects on actual system.

Status of the Program

During the last three months, a research team has been assembled and the experimental apparatus for transient and steady state air injection into an axisymmetric chamber has been designed and fabricated. The instrumentation to study vent clearing process and the surface response during steady

4

state air injection has been completed. During the reporting period considerable effort has been expended in selecting proper instruments to meet the required constraints of the experimental accuracy requirements. Calibration of flow meter and pressure transducers have been performed. However, some difficulty has been encountered in transient calibration of the pressure transducers and the response of the pressure transducers tested up to now is found to be much slower than desired. In this regard further information is being gathered before purchasing more pressure transducers which will satisfy our needs. Orders have been placed for data acquisition system and steam supply system.

Existing work on scaling of vent clearing phenomena during transient air injection has been reviewed during the reporting period. Simple model for vent clearing process and scaling laws for subsonic and sonic air discharge have been developed. Data for rate of vent clearing and total time to clear the vent has been obtained for different submergence depths and upstream pressures. Motion pictures of the vent clearing process have been made and it is observed from the pictures that considerable mass of liquid is held up at the tube wall during the ejection of the liquid slug. Data for maximum swell height have been obtained and modes of oscillations of the surface have been studied from the motion pictures. It is seen that the pool walls do have some effect on the swelling phenomena. The data for pool swell height have been correlated with Froude number.

For the next quarter, more refinements of the apparatus and instrumentation have been planned. Data for pressure forces generated on the bottom of the pool during vent clearing and data for pool free surface swelling

5

rate will be obtained. Detailed instrumentation and photographic techniques will be improved to get detailed information of the bubble behavior at the time of complete vent clearing.

2.0 SCALING AND ANALYSIS

The purpose of a scaling analysis is to provide a theoretical base relating the laboratory model experiment to the full-scale prototype, to simulate the operation of the full-scale system by the model, to correlate the data gathered in the laboratory, to extrapolate the laboratory data to the prototype, and to identify all of the significant parameters. There are two fundamental questions that must be resolved before a scaling analysis can be initiated:

(1) Which part of the LOCA experiment is to be simulated in the laboratory?

(2) How are the parameters that must be simulated in the laboratory experiments identified?

For the BWR containment system, it is believed that a single apparatus can not simulate all phases of LOCA. Scaling for vent-clearing, sonic and subsonic discharge of compressed air (or steam) by a single experiment will, in our view, be quite difficult, if not impossible to simulate. In other words, the entire LOCA can hardly be simulated in any realistic fashion by affixing a single set of parameters, irrespective of whether the model is 1/5 or 1/12 linear dimension of the prototype. In a laboratory experiment, there are realistic limits in the range of temperature, pressure, time-scale, and the sensitivity of instruments (such as pressure transducers) that must be recognized.

As to the method of analysis, one must distinguish between dimensional analysis and simulitude. Dimensional analysis consists of compiling a list of relevant physical variables, then applying the Buckingham Pi theorem to yield certain dimensionless groups. Simulitude consists of identifying those groups through normalizing the governing equations and their associ-

ated boundary and initial conditions. The method of simulitude will be used in this work.

In the present analysis, the initial stages of a LOCA are studied by considering three separate bases: vent clearing, sonic discharge and subsonic discharge of air. Pool swell and the estimation of downward or upward forces on the structure are natural products of the analysis. The effect of steam condensation will be included in the next period of research.

2.1 Scaling in Vent Clearing

Consider Eq. (4.1) [in section 4.1] as the sole governing equation for the vent clearing phase and introduce the following quantities as character-istic variables:

L = characteristic length,

ρ_w = characteristic density,

U = characteristic velocity

p_c = characteristic pressure

Then, the characteristic time $t_c = L/U$. Using *- superscript to denote normalized quantities, Eq. (4.1) in dimensionless form[+] becomes

$$[1+(\beta-1)x^*]\,\frac{du^*}{dt} + \beta u^* = \frac{p_c}{\rho_w U^2}\,p^*_D - \frac{gL}{U^2}\,x^* \tag{2.1}$$

Two dimensionless groups appear in Eq. (2.1); the Froude number gL/U^2 and the Euler number $p_c/\rho_w U^2$. Simulitude requires that

$$\left(\frac{gL}{U^2}\right)_p = \left(\frac{gL}{U^2}\right)_m \quad \text{and} \quad \left(\frac{p_c}{\rho_w U^2}\right)_p = \left(\frac{p_c}{\rho_w U^2}\right)_m \tag{2.2}$$

Subscripts p and m represent quantities for the prototype and the model respectively. Simulitude in the Froude number leads to the required scal-ing of the characteristic velocities,

---

[+] Refer to section (4.1) for detailed explanation of the notation.

8

731 003

$$U_p/U_m = \sqrt{L_p/L_m} \tag{2.3}$$

It, in turn, determines the scaling of pressure and time

$$\frac{p_{c,p}}{p_{c,m}} = \frac{L_p}{L_m} \quad \text{and} \quad \frac{t_{c,p}}{t_{c,m}} = \sqrt{L_p/L_m} \tag{2.4}$$

Assuming a 1/12 scale experiment, we find that the pressure simulation would not be realistic if $p_{c,p}$ is of the order of one atmosphere and the working medium is water. On the other hand, a 1/5 scale experiment is possible provided that proper attention is directed to the sensitivity of the pressure transducers.

2.2 Discharge of Compressed Air

Fluid motion in three different regions of the wet well is governed by three different sets of equations. Air in the top air space above water is considered to undergo an isentropic process. The volume of the top air space V_1 is given by

$$V_1 = V_{Total} - V_w - V_{III} \tag{2.5}$$

hence

$$p_1 V_1^\gamma = p_{10} V_{10}^\gamma \tag{2.6}$$

where

V_{Total} is the total volume of the wet well,

V_w is the total volume of water in the wet well, and

V_{III} is the volume of the air bubble.

The subscript o denotes some reference condition for the air.

The motion of water in the wet well is governed by the conventional equations of continuity and momentum.

$$\frac{1}{r}\frac{\partial}{\partial r}(ur) + \frac{\partial v}{\partial z} = 0 \tag{2.7}$$

9

$$\frac{\partial u}{\partial t} + u\frac{\partial u}{\partial r} + v\frac{\partial u}{\partial z} = -\frac{1}{\rho_w}\frac{\partial p_w}{\partial r} \tag{2.8}$$

$$\frac{\partial v}{\partial t} + u\frac{\partial v}{\partial r} + v\frac{\partial v}{\partial z} = -g - \frac{1}{\rho_w}\frac{\partial p_w}{\partial z} \tag{2.9}$$

where u and v are velocity components in the r and z directions respectively, p_w is the pressure of water in the wet well. The associated boundary conditions are that the pressure at the interface between the top air space and the water, and at the bubble surface are matched.

The air bubble, which is assumed to be spherical with a radius r(t), has a uniform density ρ_b and pressure p_b.[+] Conservation of air mass inside the bubble is given by

$$\frac{d}{dt}\left(\frac{4}{3}\pi\rho_b r^3\right) = \dot{m} , \tag{2.10}$$

with the air mass flux $\dot{m}$ into the bubble given by, for the sonic discharge case,

$$\dot{m} = A\sqrt{\gamma(2/\gamma+1)^{\gamma+1/\gamma-1}p_s\rho_s} , \tag{2.11}$$

where A is the cross-sectional area of the downcomer and the subscript s denotes stagnation conditions at the dry well. The formula for $\dot{m}$ is valid for sonic discharge, when the ratio of pressure at the wet well to that at the dry well is below the critical value (0.528 for $\gamma = 1.4$).

The air in the bubble is described by the ideal gas law

$$p_b = \rho_b RT_b \tag{2.12}$$

The energy equation for air in the bubble,

[+]Conclusions herein are unaltered for non-spherical expansion.

731 085

$$C_v \frac{d}{dt} (\rho_b V_b T_b) = C_p T_3 \dot{m} - (p_b - p) \frac{dV_b}{dt} \qquad (2.13)$$

Time rate of	Energy	Work done by expansion
change of in-	flux com-	of air in the bubble
ternal energy	ing into	against the background
	the bubble	pressure p .

in which

V_b = volume of the bubble = $\frac{4}{3} \pi r^3$

T_3 = temperature of air at the downcomer exit = $\frac{2}{\gamma+1} T_s$

T_s = stagnation temperature of air in the dry well.

Introducing pressure, z, L, U, p_c, ρ_c, and T_c as the characteristic length, velocity, pressure, density, and temperature respectively into the governing equations and normalizing, three groups of parameters are found; the Froude number gL/U^2, the Euler number $p_c/\rho_c U^2$ and the new Mach number $U^2/\gamma RT_c$. Hence, for simulation of sonic discharge for the prototype by the model, it is required that the velocity ratio be

$$\frac{U_p}{U_m} = \sqrt{L_p/L_m} \qquad (2.14)$$

the temperature ratio to be

$$\frac{(RT_c)_p}{(RT_c)_m} = \frac{L_p}{L_m} \qquad (2.15)$$

and the pressure ratio to be

$$\frac{p_{c,p}}{p_{c,m}} = \frac{L_p}{L_m} \qquad (2.16)$$

With the exception of the temperature ratio, scaling requirements in the sonic discharge phase are identical to those required for the vent-clearing stage. The requirement on the air temperature in the model is difficult to meet for a 1/12 scale experiment, or even the 1/5 scale experiment. Simulation in the sonic discharge regime may require the usage of a different working medium than air. The Mach number could be made similar

11

731 036

by using a gas with a substantially different gas constant. It is, however, tempting to seek a convenient argument that the sonic discharge period is short enough to be disregarded.

As the pressure in the wet well decreases, the air discharges would no longer be sonic and the mass flux in the subsonic flow becomes

$$\dot{m} = A \, \rho_h \, [\frac{2\gamma}{\gamma-1} \frac{P_s}{\rho_s} (1- \frac{P_b}{P_s} \frac{\rho_s}{\rho_b})]^{1/2} \tag{2.17}$$

It can be readily shown that the same set of dimensionless parameters would result for the subsonic discharge stage as in the sonic phase.

Simple analytical solutions, like that in the vent-clearing case [Section 4.1], have also been obtained for both sonic and subsonic discharges. Those solutions are useful particularly in bringing out the fundamental physics of the problem, and in comparing them with numerical computations. They are to be detailed in the next progress report.

12

3.1 Description of the Experiment

A schematic diagram and a photograph of the experimental apparatus used to determine the time rate of vent clearing, total vent clearing time and steady state swell height are shown in Figures 3.1 and 3.2. The apparatus consists of a cylindrical test chamber and an air supply which is composed of a reservoir connected to the test chamber through a 51 mm nominal diameter pipe.

The test chamber is made of a plexi-glass pipe 45 cm in diameter and 120 cm in height. The plexi-glass pipe is held at the ends with two air tight flanges made out of 2.5 cm thick aluminum plate. The bottom flange has two holes for connecting the test chamber to a fresh water supply and to drain. Five holes 6 mm in diameter are tapped in each of the two diametral planes of the bottom flange for placing pressure transducers, see Figure 3.3 . A 51 mm diameter tube holder is welded to the top flange through which tubes of up to 47 mm diameter can be inserted into the test chamber. Ten holes of 19 mm diameter are also tapped in the top flange. These holes are generally open to the atmosphere but can be closed when the experiments are to be conducted at pressures other than atmospheric.

The tube holder on the upper flange is connected to the 51 mm diameter air supple line via a Thermo Systems Model 4100-1 digital flowmeter. The analog response time of the flowmeter is 2 milli-seconds and the flowmeter is capable of measuring a maximum velocity of 50 M/s with an accuracy of $\pm$ 2%. A Celesco inductive type pressure transducer is placed downstream of the flow meter to measure line static pressure. The response time of the pressure transducer is suggested by the vendor to be 1 milli-second, although laboratory calibration showed the responce of the pressure transducer to be much slower. A more detailed discussion of the calibration procedure is presented in Appendix A. The analog output of the pressure trans-
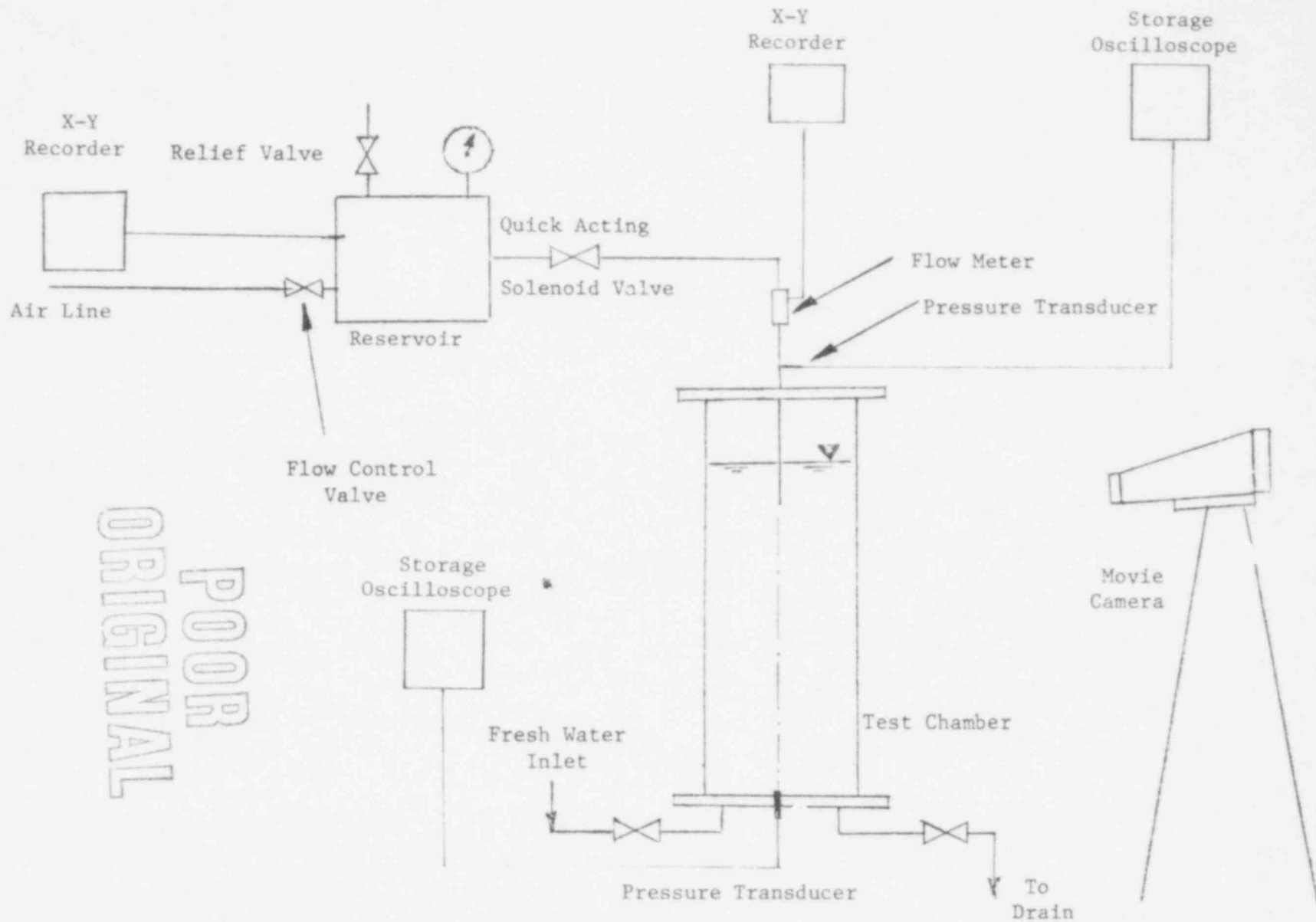
Figure 3.1. Schematic Diagram of the Apparatus

14

731 089
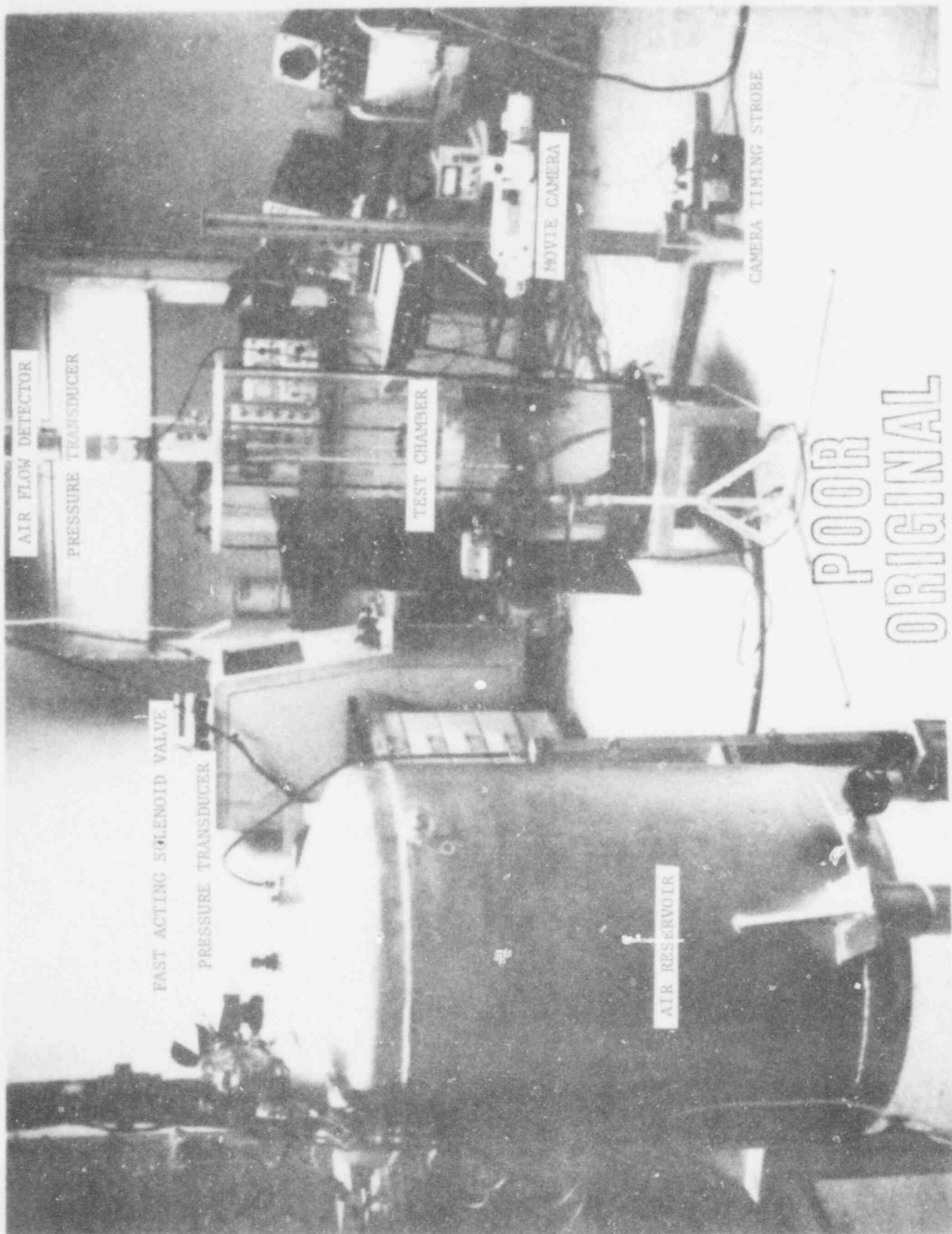
Figure 3.2 Photograph of the Apparatus

AIR FLOW DETECTOR

PRESSURE TRANSDUCER

FAST ACTING SOLENOID VALVE

PRESSURE TRANSDUCER

TEST CHAMBER

MOVIE CAMERA

CAMERA TIMING STROBE

AIR RESERVOIR

POOR ORIGINAL

178

— 54 —

— 38 —

19

70

— 108 —

269

295

— 75 —

— 38 —
— 54 —
— 70 —

— 108 —

9.5 mm
Tapped hole

61
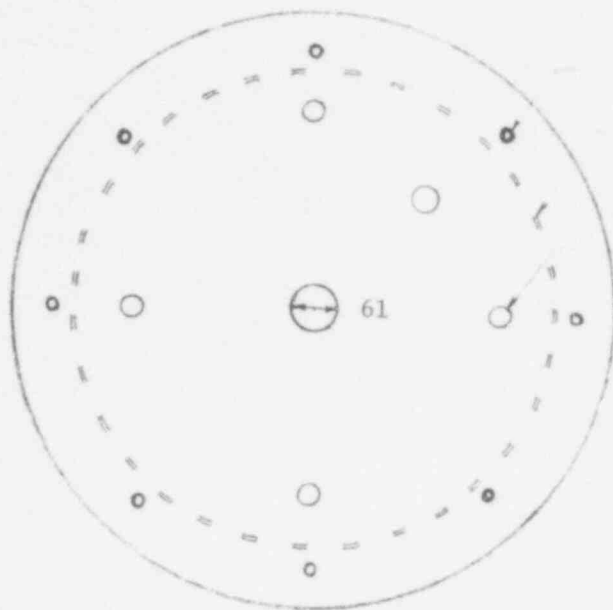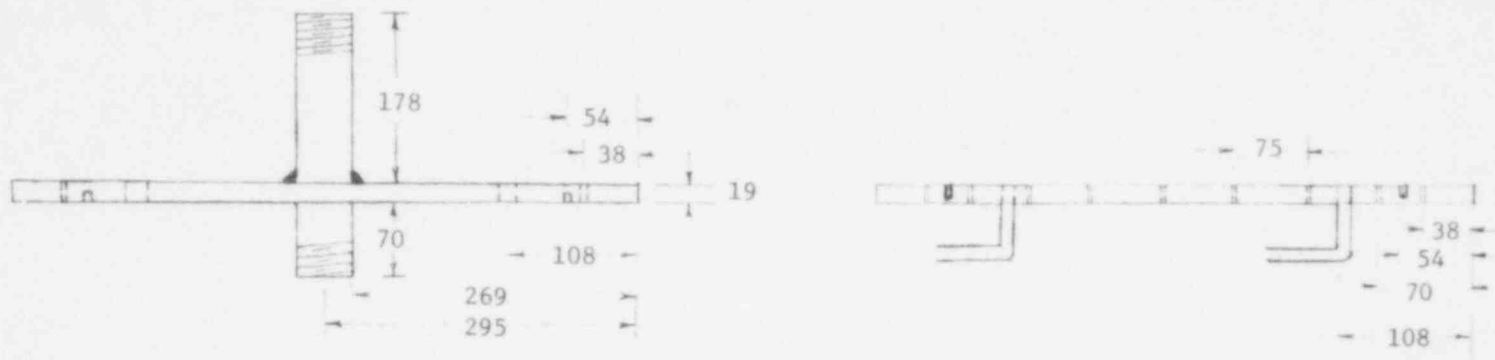
25 mm
Tapped hole

12.5 mm
Tapped
Hole

25 mm Tapped
Hole

TOP FLANGE

BOTTOM FLANGE

All dimensions in mm

Figure 3.3.   Scaled Drawing of the Top and Bottom Flanges of the Test Chamber

From air
supply

water
level

He-Ne laser

Prism

Front
silvered
mirror
(plane)

Photomultiplier

Signal
Output

Taktronic 564
Storage Scope

POOR
ORIGINAL

19

731 092
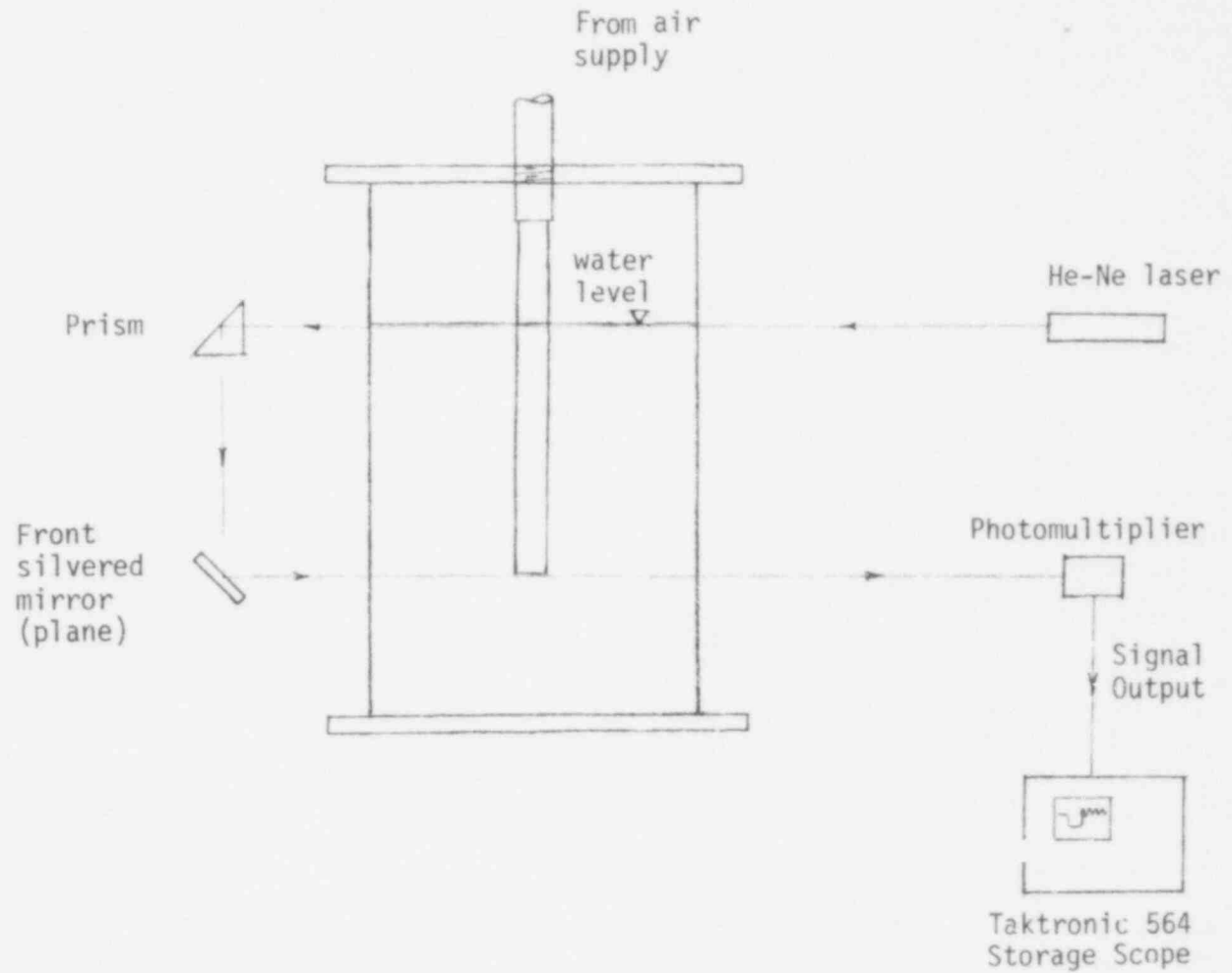
Figure 3.4 Laser System for Vent Clearing Time Measurement

rate of air was maintained through the vent. In these experiments the controllable parameter was the average flow velocity and its maximum value was limited by the capacity of the laboratory utility air supply system. The data for the swell height was again taken on fast movie film at a maximum speed of 780 frames/second with an exposure time of 500 micro-seconds. The experiments were repeated when the average air flow velocity through the vent was varied from 20 cm/sec to 350 cm/sec.

3.3 Data Reduction

Photographic information was used to determine the rate of vent clearing, total time to clear the vent, maximum pool free surface swell height and the mode of free surface oscillations.

The 16 mm movies were first projected on a screen and preliminary survey was made to determine the portions of interest. The film was then transferred to a micro-fiche reader. Starting from a frame in which the interface had just moved, the location of the interface was measured from the tube exit plane. The number of frames were then counted during which the interface moved a certain distance. The exact frame speed during this period was determined from the neon light marks on the film.

A similar procedure was used to reduce the data from movies for free pool surface swell height during steady state injection. While making these observations it was very difficult to ascertain the pool surface mean height because of the presence of large disturbances at the free surface. Thus, the reported values of the maximum swell height are measured from the original undisturbed pool height.

ducer is supplied to a Tektronic 564 Storage Oscilloscope. The time response of this oscilloscope is 0.5 micro-seconds.

The air reservoir is a cylindrical steel tank 0.3 m^3 in volume. The safe working pressure for the reservoir is 200 kPa and is controlled by actuation of a safety relief valve attached to the vessel. The pressure inside the vessel is read by a Bourden type pressure gage and by a Celesco strain gage type pressure transducer. The pressure transducer signal is recorded on a Hewlett Packard Mosley X-Y recorder. The reservoir can be pressurized by opening a solenoid valve connected to utility air supply system of the laboratory. A 37 mm diameter quick acting solenoid valve connects the reservoir to the test chamber through the 51 mm nominal diameter pipe line. The solenoid valve opens completely, 32 to 64 milli-seconds after actuation of the valve.

In addition to the movie technique, a laser system was set up as an alternate means to measure the vent clearing time as shown in Figure 3-4. The laser beam from a 15mW He-Ne laser is directed through the test chamber and the glass tube at a lever just below the air-water interface. The beam is redirected downward by a glass prism to a front surface silver mirror which reflects the beam back to the test chamber at such level that the beam just clears the glass tube. The laser beam intensity is detected by a silicon photo-multiplier. The signal from the photo-multiplier is recorded by the Taktronic 564 storage Oscilloscope.

At present the phenomenon of bubble growth at the pipe exit have not been studied in detail. An improved high speed photographic technique based on the work of Arakeri et al. [2], will be employed to study the interfacial phenomenon. This method is described in Appendix B.

3.2 Procedure

Before starting an experiment, the flowmeter, pressure transducers, recorders and movie camera were synchronized and their operability checked. A desired size pyrex glass tube with a centimeter scale pasted to it was inserted through the tube holder in the upper flange and held rigidly to the flowmeter gun. The tube length in most of the tests was nearly 1.0 meter which made the exit plane of the tube to be about 20 cm from the bottom of the test chamber. The test chamber was then filled with fresh water to allow a pre-selected depth of submergence. The air reservoir was then pressurized. The quick-acting solenoid valve was then opened and all other systems including the Photosonics movie camera activated. The vent clearing process was captured on a fast movie film at a maximum speed of about 780 frames/second and exposure time varying from 500-63 micro-seconds. After the reservoir emptied, the pool was allowed to reach its undisturbed position and the experiment was repeated with a different maximum reservoir pressure. In this study the vent clearing data were taken for tubes of 21, 34 and 47 mm diameter, when the reservoir maximum pressure was varied from about 2 psig to about 7 psig and the submergence depth was varied from 10 cm to 60 cm.

In determining the vent clearing time by the laser technique, similar procedure is followed for the air injection. The oscilliscope is triggered automatically once the valve starts to open. The interruptions of the laser beam by the interface firstly when it passes through the upper beam and secondly, when it passes through the lower beam (Figure 3.4), produce two distinct signals on the oscilloscope. The vent clearing time can then be reduced by these two signals since the sweeping speed of the oscilloscope is known.

The swell height experiments were conducted when a steady state flow

731 095
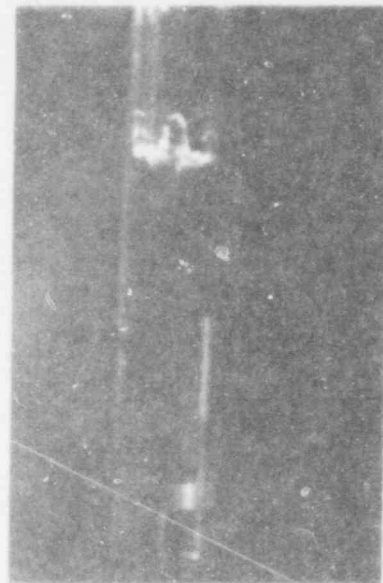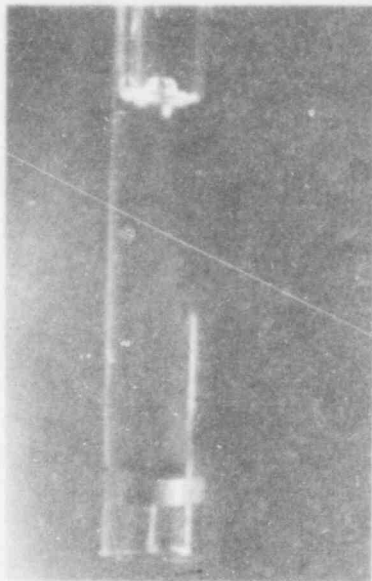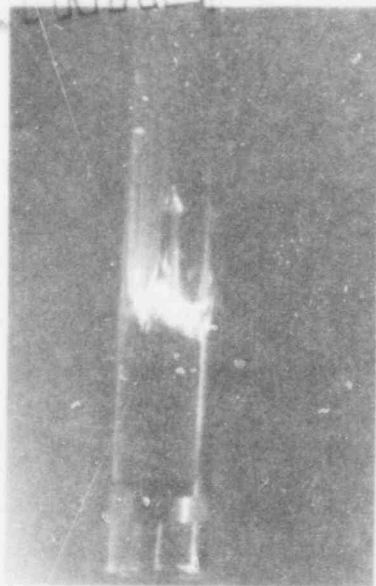
Figure 4.1
Vent clearing showing formation of interface instability.
Vent Diameter = 4.6 cm
Upstream Air Pressure = 3 psig
Submergence Depth = 30 cm
Exposure Time = .001 sec.

731 096

4.1 Vent Clearing Phenomenon

Visual Movie Observations

Immediately after the valve opening, the inflow of pressurised air is observed to form a depression in the liquid surface. At the same time, the liquid column is accelerated and pushed into the water pool. During the processes of injection a liquid film is seen to adhere to the tube wall upstream the air-water interface, due to the no-slip boundary condition at the tube wall. The amount of liquid in the film is observed to be a function of the upstream pressure conditions. As the interface moves downward, the Kelvin Holmholtz phenomenon strips globules from the liquid film surface and the globules are entrained in the gas stream, forming a two phase region. In addition, the Taylor instability resulting from the high acceleration of the liquid column in the tube breaks up the interface as shown in the sequential pictures in Figure 4.1. These observations are quite contrary to conventional modelling of the vent clearing where the air-water interface is assumed to be distinct and flat. Further interpretations of the results will be reported later.

Theoretical Considerations

The transient motion of the water slug in the vent during the vent clearing transient is usually assumed to behave as a rigid body [1]. The forces acting upon it are assumed to be the drywell pressure (P_D), the friction force due to the walls of the vent, the weight of the water slug and the back pressure exerted by the liquid (ρL) and gas (P_w) within the well well at the vent pipe exit plane. The apparent mass effects resulted from fluid motion which have always been neglected, are to be studied in the present analysis. From the force balance on the water mass (Figure 4.2), the momentum equation is given by

$$\frac{d(mu)}{dt} + \rho_w u^2 A = [(P_D - P_s) - \rho_w x]A - \frac{f_m(L - x)u^2 A}{2d} \tag{4.1}$$

21

731 097
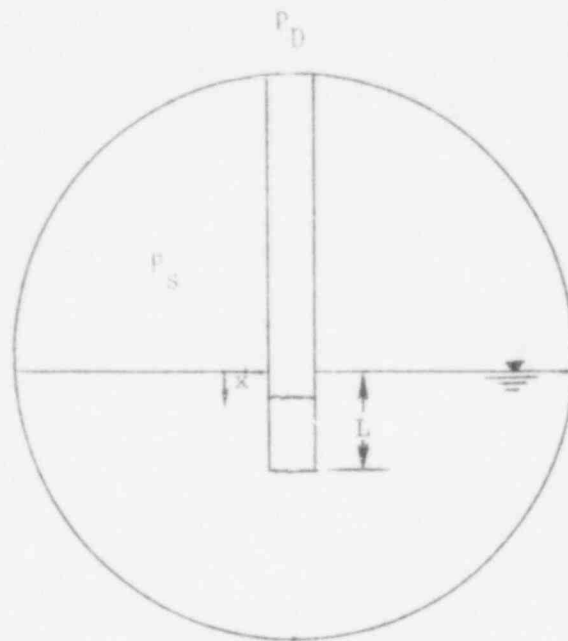
Figure 4.2 Physical Model for Vent Clearing

23

731 098

where x is the interfacial location (Figure 4.2) and it is related to the slug velocity u by

$$\frac{dx}{dt} = u \qquad (4.2)$$

where

       P   is the pressure
       L   is the submergence depth
      ρ_w is the water density
      A   is the pipe area
      d   is the pipe diameter
      t   is the time
      f_m is the Fanno friction factor

    m is the total mass. It is composed of two parts, the real mass during the transient, i.e. $\rho(L - x)A$ and the apparent mass m_{ao} . In the analysis the apparent mass is assummed to be a linear function of x , i.e.

$$m_{ao} = \beta \rho_w A x \qquad (4.3)$$

where β is a proportionality constant and it will be shown of unity one. For example, a ellipsoid of evolution, the apparent mass for moving in the major axis (a) direction is given by

$$m_{ao} = \frac{\alpha_o}{2 - \alpha_o} \ \frac{4}{3} \ \pi(abc)\rho_w \qquad (4.4)$$

where

    a, b, c are the semi-axes of the ellipsoid; α_o is related to a, b, and c by

$$\alpha_o = a\,b\,c \int_0^\infty \frac{d\lambda}{(a^2 + \lambda)^{3/2} \sqrt{(b^2 + \lambda)(c^2 + \lambda)}} \qquad (4.5)$$

which is an elliptic integral [4].

For spheres of radius a

$$m_{ao} = \frac{2}{3} \rho_w \pi a^3 \qquad (4.6)$$

For disk of radius a

$$m_{ao} = \frac{8}{3} \rho_w a^3 \qquad (4.7)$$

    It is based on the results of these geometries that it is concluded that β is of the order of unity. In the actual vent clearing case, β is

expected to be a function of time, the solution of this actual β requires a complete solution of the transient fluid motion inside the vent and the pool. The solution is not attempted at this stage. However, the effect of β on vent clearing phenomena can be studied parametrically by solving equations (4.1) and (4.2), with specified dry well pressure P_D . Figure 4.3 shows the effect of β on the interface location for various ΔP . The interface m. , much faster for smaller β . The solid lines are computed for ΔP of 5 psig. The interfacial motion denoted by x/L can be approximately correlated by the single non-dimensional parameter $t\sqrt{2\Delta P g_c/(\rho_w L^2)}$ as demonstrated by comparing the results for 8 psig, 5 psig and 2 psig, shown in Figure 4.3. In other words, the time for the interface to be cleared of the pipe (when $x/L = 1$) decreases with the square root of ΔP but increases linearly with L . Actually, the dependence of the vent clearing time on the pressure and the submergence depth are more sophisticated depending on the pressure difference and the submergence depth. Figure 4.4 shows the variation of the non-dimensional vent clearing times $t\sqrt{2\Delta P g_c/(\rho_w L^2)}$ as functions of the pressure difference. For large ΔP , the gravitational term in equation (4.1) is less important and the term $t\sqrt{2\Delta P g_c/(\rho_w L^2)}$ remains constant. Similarly for small submergence coupled with fairly large ΔP , the vent clearing time is again proportional to $L/\sqrt{\Delta P}$ (Figure 4.5).

The effects of β on the actual vent clearing time in a BWR system are demonstrated by using the transient drywell pressure given in the FSAR of Vermont Yankee. [3]. The diameter of the vent is 2 ft and the submergence depth is 5 ft. As β increases, the velocity of the water slug is found to be decreased (Figure 4.6).

β is found to have a more dra. '. effect on the velocity when the vent starts to .lear. As β increases the velt .ity is found to be decreased.
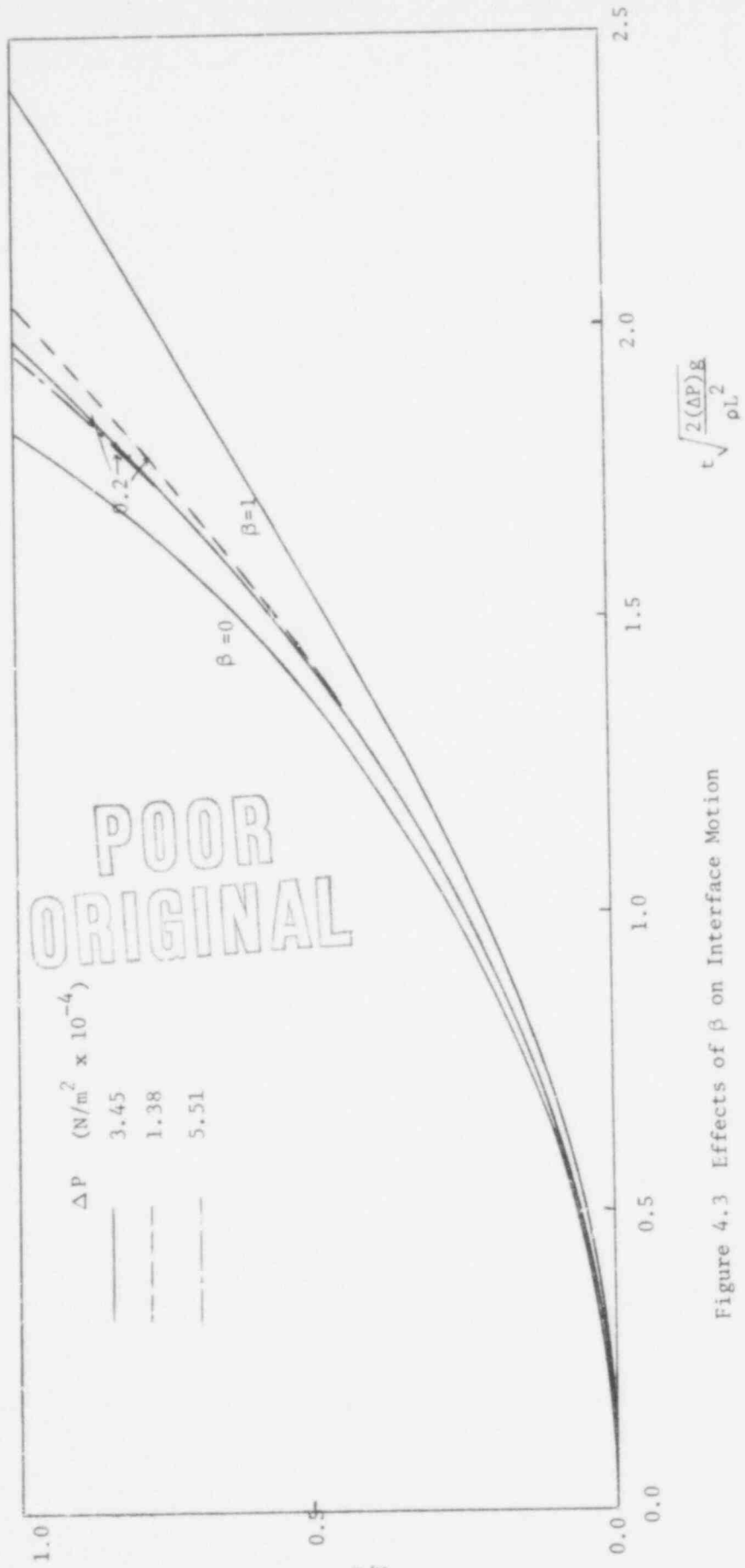
Figure 4.3 Effects of β on Interface Motion

731 101
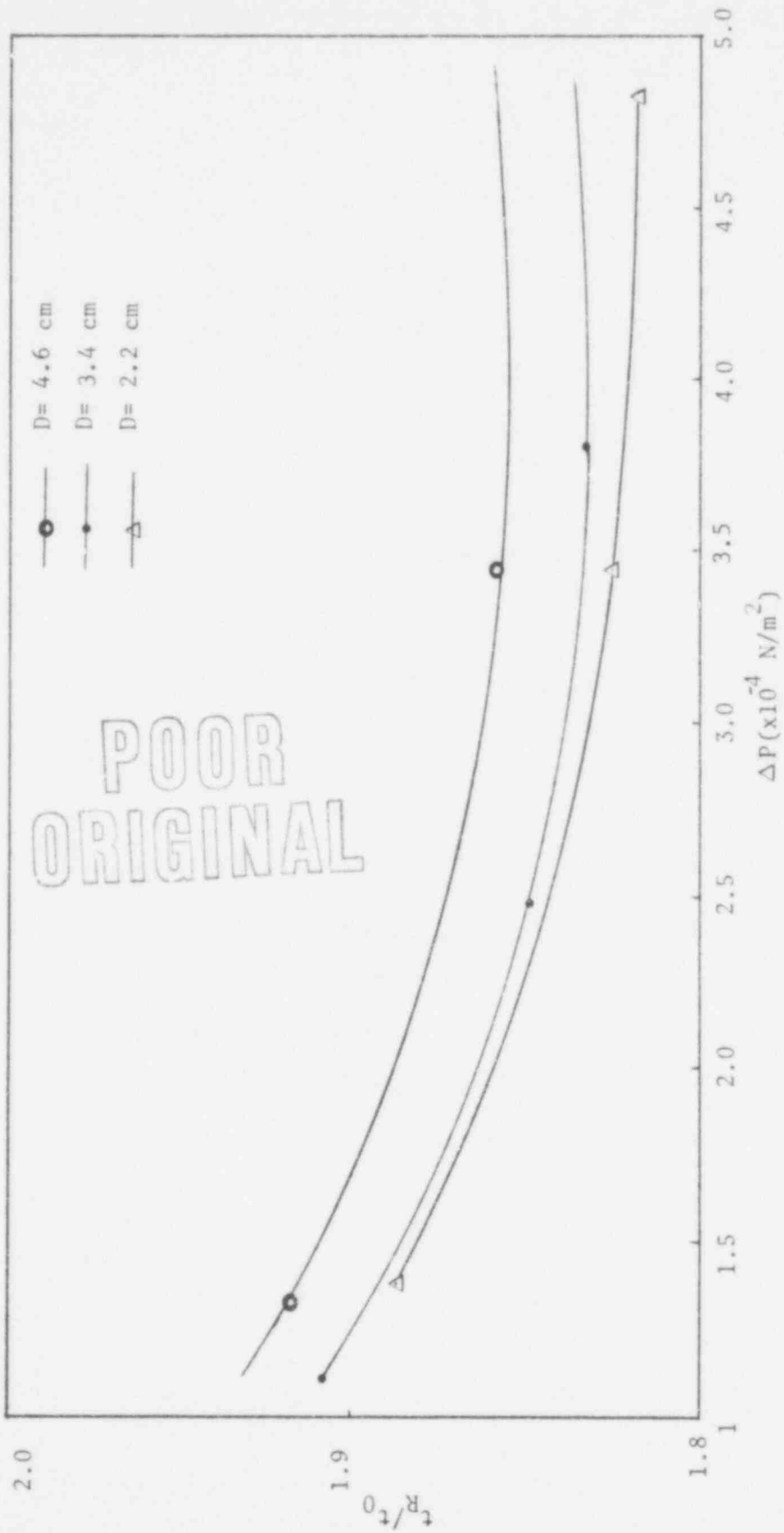
Figure 4.4 Effect of ΔP on Non-dimensional Vent Clearing Time
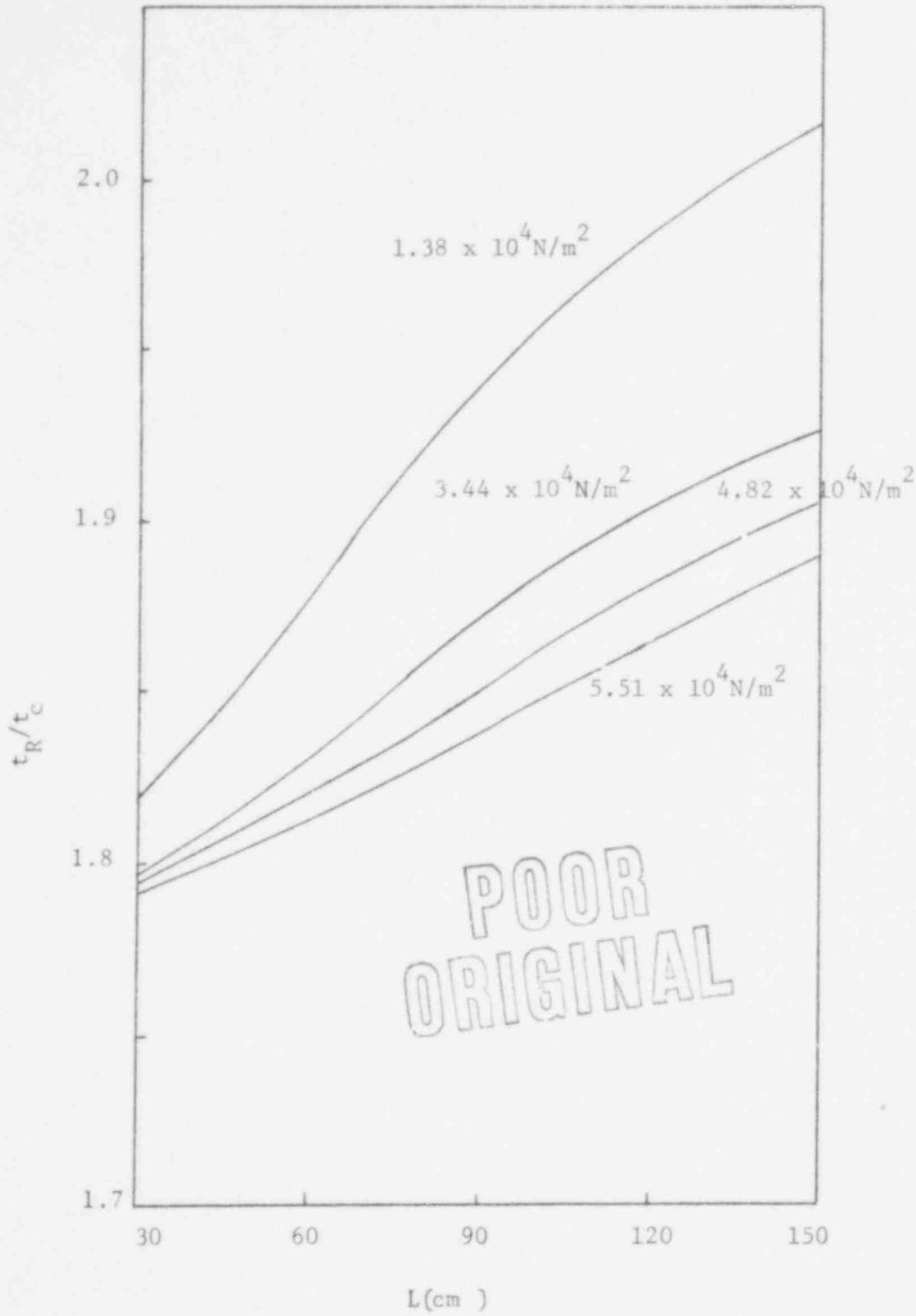
Figure 4.5 Effect of Submergence Depths on Non-dimensional Vent Clearing Time

731 103
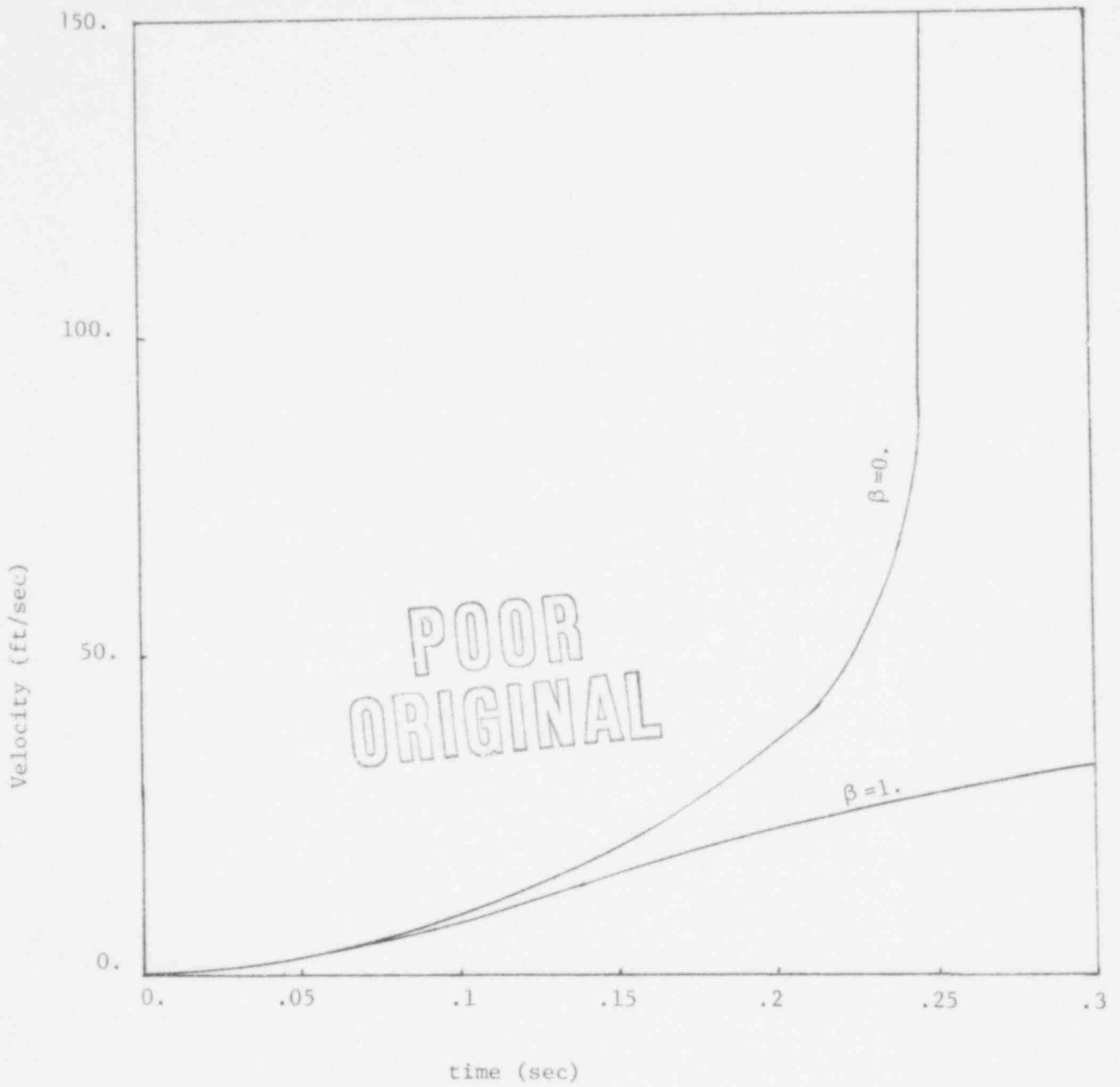
Figure 4.6 Effect of β on slug velocity

Then it reaches an asymptotic value for β greater than 0.5. The non-dimensional exit velocity is the ratio of the exit velocity over the velocity when $\beta = 0$ (Figure 4.7).

Hence the virtual mass can have two opposite effects on vent clearing phenomenon. A high β means longer vent clearing time and hence a higher pressure whe the bubble starts to grow. On the other hand, the virtual mass effect tends to slow down the exit velocity. The combined effects of the virtual mass on the dynamical forces need further investigations.

Experimental Data

In the experiments, the movement of the interface between the liquid and the two phase regions was deduced from the high speed movies. The results are shown in Figure 4.8 and for various tube sizes, driving pressures, and submergence depths. The data are summarised in Appendix C.

In spite of the data scattering, the interface movement observed in the experiment shows the same trend as predicted from the theory. The theoretical data is obtained by solving equations (4.1) and (4.2) with $\beta = 0$.

However, experimental data indicate that x/L cannot simply be correlated just with a single parameter $t\sqrt{2\Delta Pg/(\rho_w L^2)}$. As pressure increases, better comparison is obtained between the theory and the test data (Figure 4.8). Test data also exhibit the same dependence on the submergence depth as predicted from the theory (Figure 4.9).

Data for the vent clearing times are also summarised in Appendix C. The time t_1 refers to the time when the interface between the liquid and the two phase region clears out of the pipe while t_2 is the vent clearing time for the interface between the two phase region and the gaseous region; t_3 is the clearing time determined by the laser technique and t_4 is the
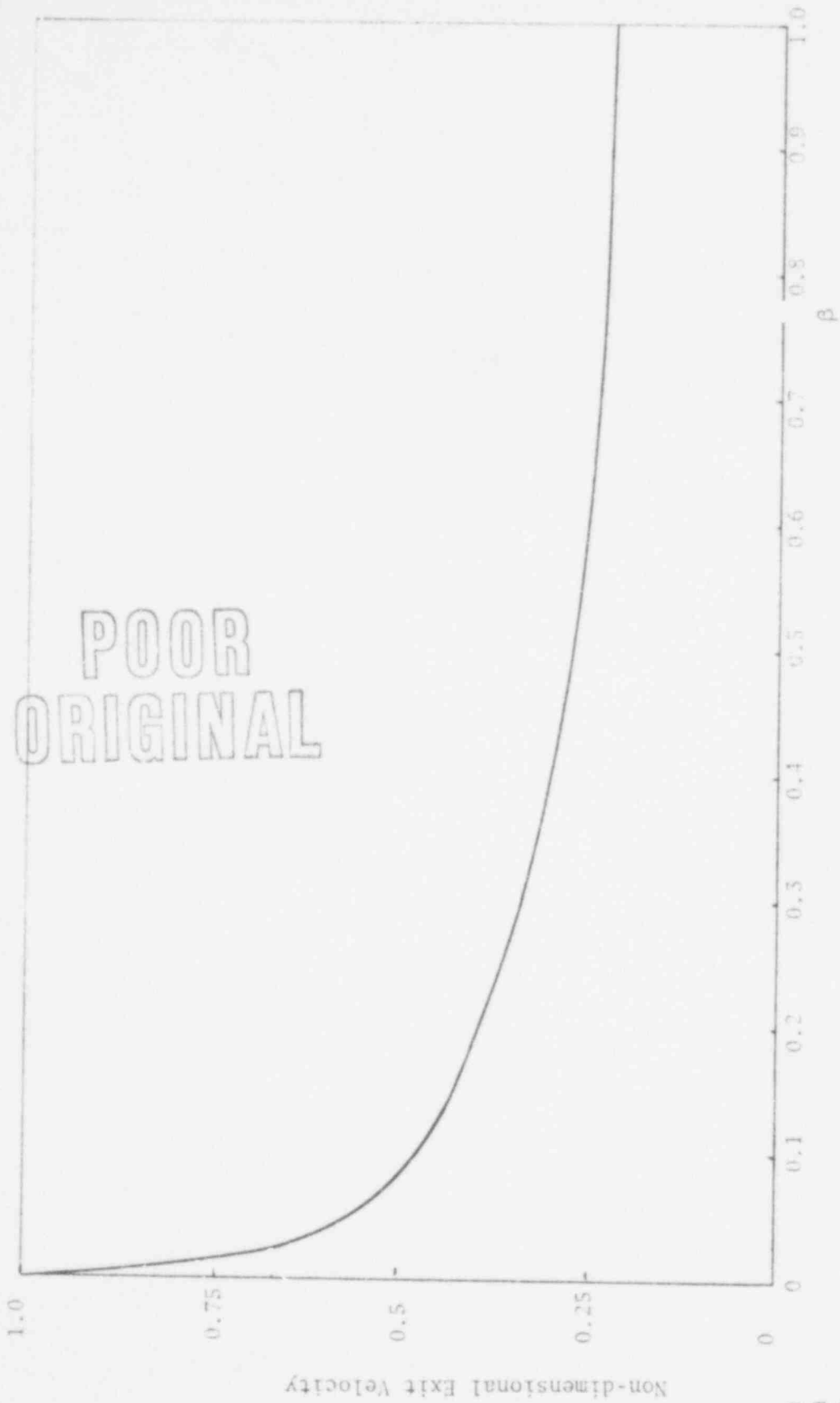
Figure 4.7 Effect of β on Exit Velocity

31

Dimensionless Position, x/L

$t\sqrt{\dfrac{2(\Delta P)g}{\rho L^2}}$

d (cm)	L (cm)	ΔP (N/m^{2}x10^{-4})	
×	2.2	60	1.52
△	2.2	60	2.56
▽	2.2	60	3.45
◐	3.4	60	1.10
◄	3.4	60	2.48
◑	3.4	60	3.79

— — EQ(1) and (2)

Dimensionless Position, x/L

$t\sqrt{\dfrac{2(\Delta P)g}{\rho L^2}}$

d (cm)	L (cm)	ΔP (N/m^{2}x10^{-4})	
+	2.2	10	0.69
◐	2.2	10	2.48
△	3.4	10	0.62
◯	3.4	10	1.03
▽	3.4	10	1.79
▲	4.6	10	0.76
•	4.6	10	1.10
▼	4.6	10	1.31
◊	4.6	10	1.45

— — EQ(1) and (2)

Figure 4.8 Air-water Interface Location as Functions of Time

32
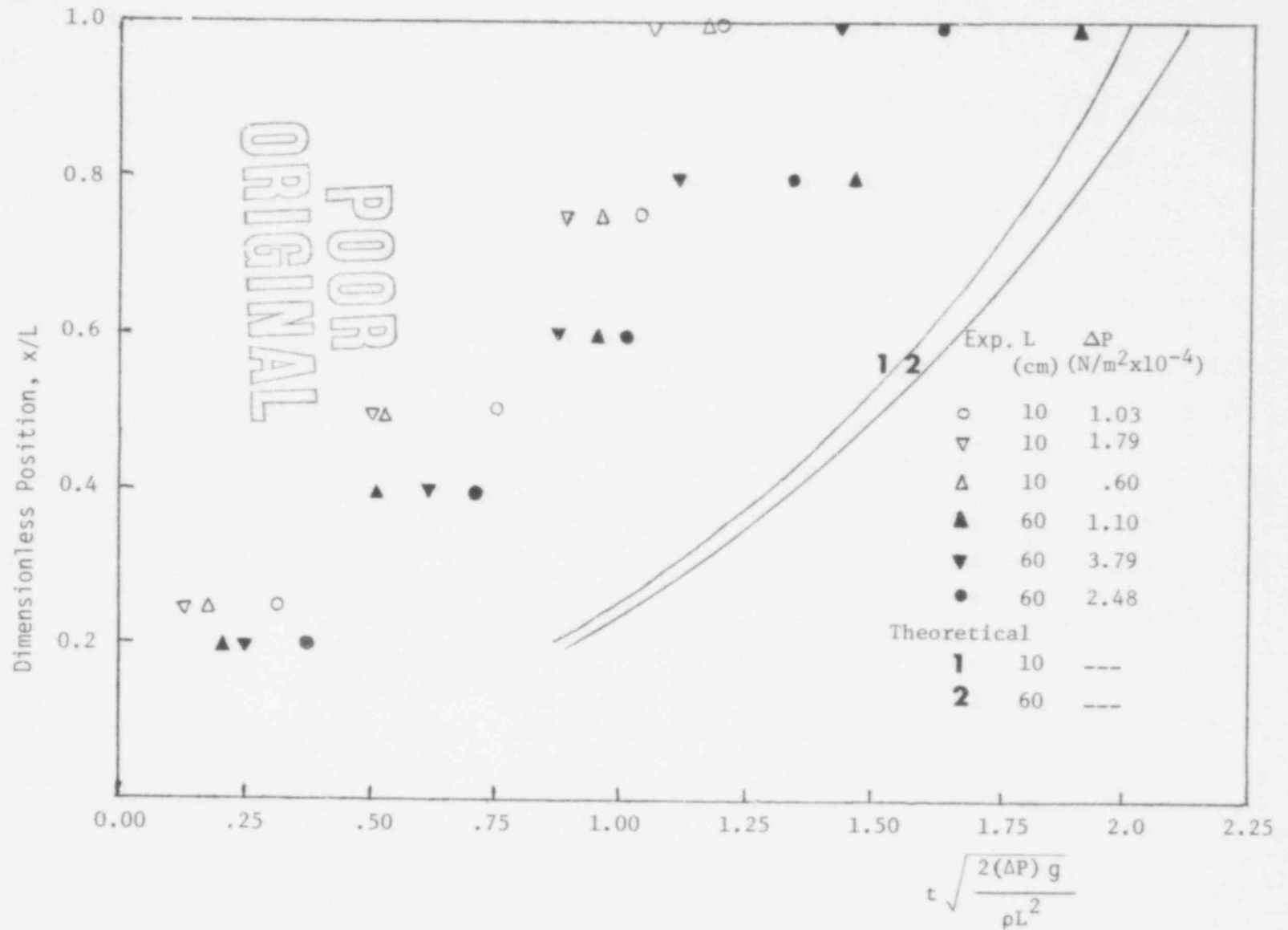
Figure 4.9   Effects of Submergence Depths on Air-Water Interfacial Motion

theoretical vent clearing time. Some of the data show that the vent clearing time predicted from the theory, i.e. the time when all the water is expelled from the vent, is lying between these two times. This two phase phenomenon would be of significance in predicting the vent clearing time in an actual BWR system.

5.0 REFERENCES

1. C. F. Carmichael and S. A. Marko, CONTEMPT-PS--A Digital Computer Code for Predicting the Pressure-Temperature History Within a Pressure Suppression Containment Vessel in Response to a Loss-of-Coolant Accident. IDO-17252, Idaho Nuclear Company, April 1969.

2. V. H. Arakeri, I. Catton, W. E. Kastenberg and M. S. Plesset, An Experimental Study of the Thermal Interaction for Molten Tin Dropped into Water, UCLA-ENG-7592, December 1975.

3. Final Safety Analysis Report, Vermont Yankee Nuclear Power Plant.

4. L. M. Milne-Thomson, Theoretical Hydrodynamics, 5th ed., McMillan, New York.

731 110

APPENDIX A

CALIBRATION OF THE PRESSURE TRANSDUCER

The time response of the Celesco - inductive type pressure transducer used to measure the static line pressure prior to and during vent clearing was checked in the laboratory. A schematic diagram of the apparatus used for the purpose is shown in Figure A.1. The pressure transducer was placed about 5 cm downstream of the quick-acting solenoid valve connected to the pressure chamber. The pressure transducer was purposely placed a short distance away from the valve so as to minimize the time taken to fill the line downstream of the valve and also to reduce the error due to time dependent opening of the valve. The output signal of the pressure transducer was supplied to a Tektronic Type 564 Storage Oscilloscope. The time signal of the Oscilloscope was activated by the relay when the electric circuit of the quick-acting solenoid valve was closed to open the valve. The pressure time history as recorded on the oscilloscope for one pressure setting of the pressure chamber (5 psig) is also reproduced in Figure A1. It is observed from this figure that the pressure transducer reads the asymptotic pressure about 50-60 milli-seconds after opening of the valve. The magnitude of the asymptotic pressure is found to be within 5% of the upstream pressure. A number of such observations showed the pressure transducer response to be considerably slower than 1 milli-second as specified by the vendor. Further investigation into acquiring a reasonably reliable fast response pressure transducer is continuing.

The Thermo Systems model 4100-1 digital flowmeter was calibrated only in steady state mode against a precalibrated flowmeter. The steady state flow velocity as recorded on the analog output of the thermosystems flowmeter was found to be within ± 2%. This accuracy is within the limits set by the vendor.

36
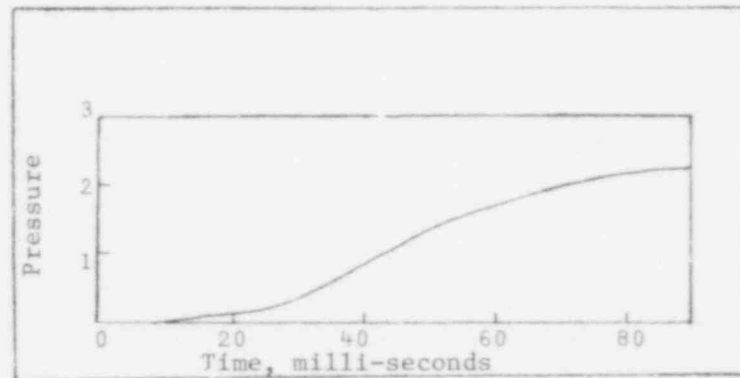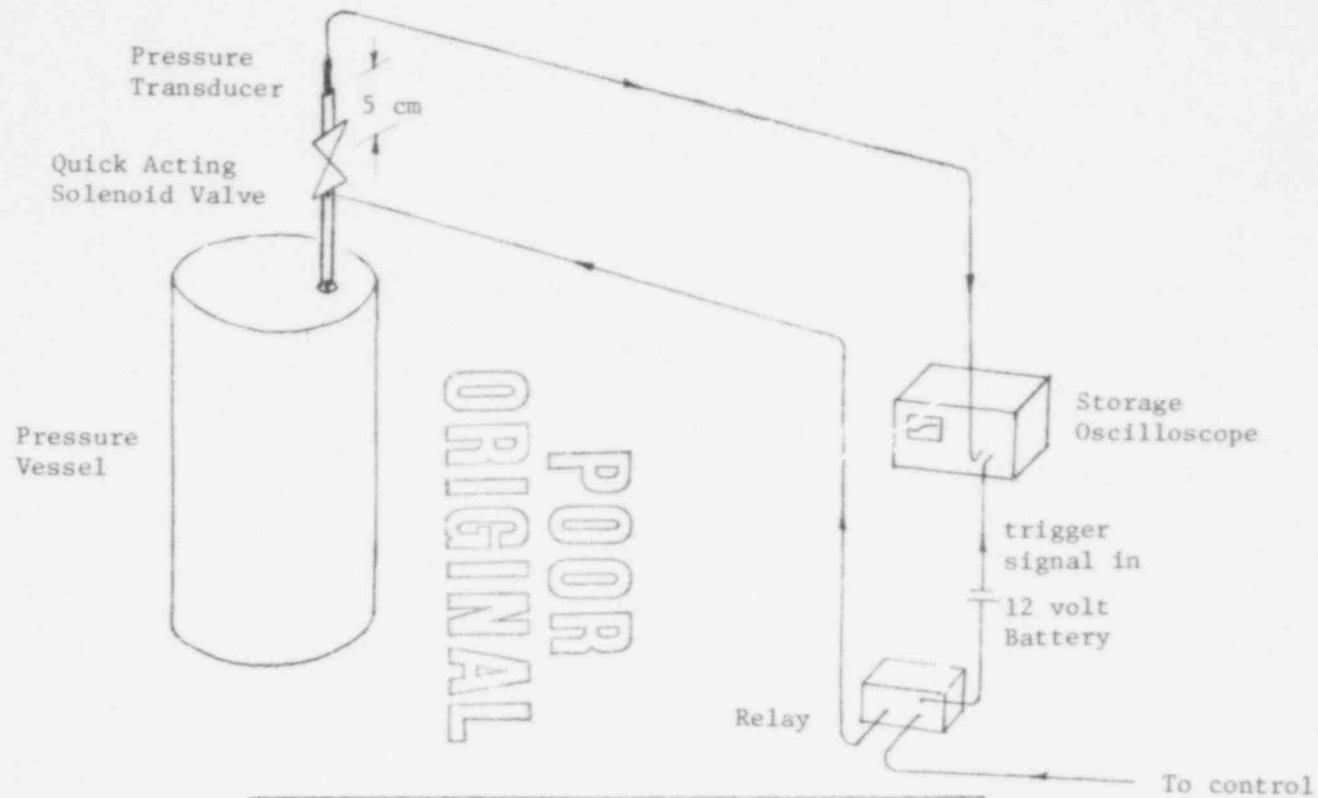
Pressure Time Response of the Pressure Transducer

Figure A.1   Schematic of the Apparatus used to Determine Time
Response of the Pressure Transducer (Celesco KP15)

731 112

APPENDIX B

PHOTOGRAPHIC TECHNIQUE FOR BUBBLE GROWTH

Arakeri et al [2] have recently developed a high speed photographic technique in their study of fuel-coolant interaction. Framing rates from 2,000 to 10,000 have been utilized and correspondingly the exposure time per frame were about 125 microseconds to about 25 microseconds at the above mentioned framing rates. In their highly transient experiment, exposure times of even 25 micro-seconds may be much too large. For this reason they utilized two General Radio stroboscopes (type 1538) which are capable of producing very short duration flashes as light sources and the experiments were performed in a completely dark space. The stroboscopes were capable of flashing at a maximum rate of 2,500 flames per second (fps) with quoted exposure time per flash of about 0.3 microseconds. At lower flashing rates of the order of 200 fps the exposure time increases to about one microsecond per flash.

Multiple flash photographs of the event were obtained by rotating a 4 inch by 5 inch (10 cm by 12.7 cm) sheet film at the image plane. A camera lens was placed at a distance of about 5 feet (1.52 m) from the object and the film was placed about 6 inches (15.25 cm) behind the lens on a disk attached to a speed controlled motor. With this arrangement it was possible to obtain about twenty-five to thirty multiple flash photographs of size of approximately half inch by half inch (1.27 cm by 1.27 cm). Typical rotation speed required was about 1725 RPM for a framing rate of one thousand photographs per second. Since very short duration flashes were involved, Kodak Royal X-Pan film with an ASA rating of 1250 was utilized to obtain adequate contrast. The film was then developed in Accufine developing solution to increase the ASA rating to about 3000.

731 113

In order to avoid overlapping of the multiple flash photographs, the flashing of the strobes to a limited number of flashes was achieved externally. First, the start up of the experiment was sensed with a photo electric pickup and the signal so produced was amplified and delayed through a delay circuit. The output from the delay circuit was used to trigger a scope which produced a negative gate. This gate was fed into an on-off circuit which also had a signal from a signal generator as a second input. The output of this circuit contained the signal from the signal generator for the limited time period when the gate from the scope had a negative going voltage. The final signal from the on-off circuit was used to drive one of the strobes and in turn the output from the first strobe was used to drive the second strobe. In order to synchronize the flashing of the strobes with the transient phenomenon in their study a delay of about 0.2 seconds to 0.25 seconds at the delay circuit was introduced. The flashing rate of the strobes was controlled by setting the frequency of the signal from the signal generator to the desired value and the number of flashes were controlled by adjusting the time width of the gate from the scope. The circuitry associated with this method of synchronizing the multiple flash photograph with the event is shown in the form of a schematic diagram in Figure B.1.

In view of their success of obtaining pictures that show distinct interface, the photo-techniques mentioned above will be applied in our air transient experiment during the stage of the bubble growth (Figure B.2). Results of using this photo-technique will be included in our next quarterly report.

731 114

39

Figure **B.1** Schematic Diagram Illustrating the Technique of Synchronizing the Multi-flash Photography with the Event.
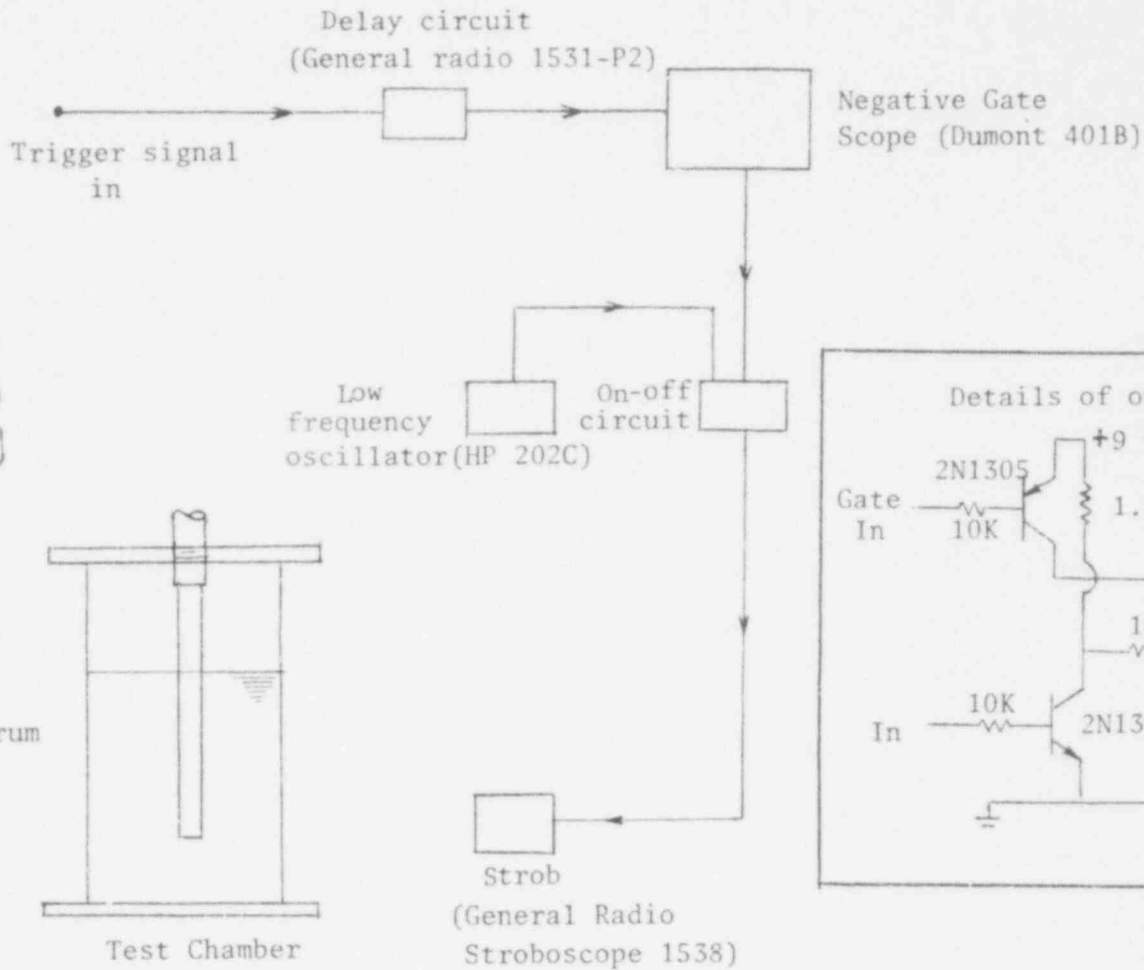
Figure B2. Schematic Diagram of photographic technique for recording bubble growth phenomenon.

41

731 116

APPENDIX C

EXPERIMENTAL DATA

This appendix documents the data for vent clearing and pool swell

height deduced from in motion pictures.

731 117

TABLE C.1

First Interface Location as Functions of Time for Tube Diameter of 4.6 cm.

p(psig)	L(cm)	t_R(sec)	t(sec)	$t^* = \dfrac{t}{t_R}$	x(cm)	$\dfrac{x}{L}$
3	30	.057	.015	.2627	6	1/5
			.0275	.4817	12	2/5
			.0375	.6569	18	3/5
			.045	.7882	24	4/5
			0.06	1.051	30	1
4	30	.0448	0.15	.335	6	1/5
			.027	.614	12	2/5
			.035	.781	18	3/5
			.045	1.004	24	4/5
			.052	1.172	30	1
5	30	.040	.0125	.3125	6	1/5
			.02	.500	12	2/5
			.03	.750	18	3/5
			.0375	.9375	24	4/5
			.045	1.125	30	1

731 113

TABLE C.1 (con't)

First Interface Location as Functions of Time for Tube Diameter of 4.6 cm.

p(psid)	L(cm)	t_R(sec)	t(sec)	t*	x(cm)	$\frac{x}{L}$
2	20	.0715	.0125	.1748	4	1/5
			.0275	.3846	8	2/5
			.045	.6294	12	3/5
			.057	.8420	16	4/5
			.065	.9091	20	1
4	20	.0317	.0125	.394	4	1/5
			.0275	.866	8	2/5
			.035	1.103	12	3/5
			.0425	1.34	16	4/5
			.0475	1.49	20	1

731 119

TABLE C.1 (con't)

First Interface Location as Functions of Time for Tube Diameter of 4.6 cm.

p(psid)	L cm	t_R(sec)	t(sec)	t*	x(cm)	$\frac{x}{L}$
2	10	.0254	.0125	.4927	3.33	1/3
			.0225	.8869	6.67	2/3
			.03	1.1825	10.0	1
3	10	.02111	.0125	.5921	3.33	1/3
			.0175	.8290	6.67	2/3
			.025	1.1843	10.0	1
4	10	.0194	.01	.5155	3.33	1/3
			.0175	.9021	6.67	2/3
			.0225	1.106	10.0	1
5	10	.0185	.01	.5417	3.33	1/3
			.015	.8126	6.67	2/3
			.02	1.083	10.0	1

TABLE C.2

First Interface Location as Functions of Time for the Tube Diameter of 3.4 cm

p(psid)	L(cm)	t_R(sec)	t(sec)	t*	x(cm)	$\frac{x}{L}$
2	60	.1277	.045	.352	12	1/5
			.0775	.602	24	2/5
			.1225	.959	36	3/5
			.175	1.37	48	4/5
			.22	1.723	60	1
4	60	.0851	.0425	.499	12	1/5
			.065	.764	24	2/5
			.085	.999	36	3/5
			.1075	1.263	48	4/5
			.1275	1.498	60	1
6	60	.0688	.0275	.399	12	1/5
			.0475	.690	24	2/5
			.0625	.908	36	3/5
			.075	1.09	48	4/5
			.0925	1.34	60	1
6	30	.04037	0.02	0.495	6	1/5
			0.03	0.743	12	2/5
			0.04	0.991	18	3/5
			0.0475	1.177	24	4/5
			0.055	1.36	30	1

731 121

P(psid)	L(cm)	t_R(sec)	t(sec)	t*	x(cm)	$\frac{x}{L}$
2	10	0.0288	0.01	0.348	2.5	1/4
			0.0175	0.608	5.0	2/4
			0.0275	0.956	7.5	3/4
			0.0325	1.13	10	1
4	10	0.022	0.01	0.455	2.5	1/4
			0.0175	0.796	5.0	2/4
			0.0225	1.024	7.5	3/4
			0.025	1.14	10	1
6	10	0.0167	0.005	.300	2.5	1/4
			0.01	.600	5.0	2/4
			0.015	.900	7.5	3/4
			0.0175	1.05	10	1

47

TABLE C.3

First Interface Location as Functions of Time for Tube Diameter of 2.2 cm

p(psid)	L (cm)	tR (sec)	t (sec)	t*	x (cm)	$\frac{x}{L}$
2	60	.1171	.045	.384	12	1/5
			.077	.662	24	2/5
			.11	.939	36	3/5
			.147	1.26	48	4/5
			.187	1.60	60	1
4	60	.0807	.04	.495	12	1/5
			.075	.929	24	2/5
			.10	1.24	36	3/5
			.1325	1.64	48	4/5
			.16	1.982	60	1
6	60	.0722	.0375	.5193	12	1/5
			.06	.831	24	2/5
			.0875	1.212	36	3/5
			.115	1.593	48	4/5
			.1375	1.904	60	1

731 123

TABLE C.3 (continued)

First Interface Location as Functions of Time for Tube Diameter of 2.2 cm

p(psid)	L(cm)	tR(sec)	t(sec)	t*	x(cm)	$\frac{x}{L}$
2	30	.0602	.0225	.374	6	1/5
			.0425	.706	12	2/5
			.0675	1.122	18	3/5
			.095	1.58	24	4/5
			.12	1.99	30	1
4	30	0.042	.0225	.536	6	1/5
			.04	.953	12	2/5
			.0525	1.251	18	3/5
			.06	1.43	24	4/5
			.08	1.906	30	1
2	10	.0269	.0125	.464	3.33	1/3
			.0225	.836	6.67	2/3
			.03	1.115	10	1
4	10	.0165	.01	.605	3.33	1/3
			.02	1.209	6.67	2/3
			.025	1.512	10	1
6	10	.0148	.0075	.529	3.33	1/3
			.015	1.058	6.67	2/3
			.02	1.41	10	1

TABLE C.4

Vent Clearing Time for Different Pipe Sizes, Submergence Depths and Upstream Pressures

Film #	L(cm)	d(cm)	ΔP(psid)	p(psid)	t_1 (sec)	t_2 (sec)	t_3 (sec)	t_4 (sec)
9-30-0-1	10	3.4	.875	2	.033	.042	---	.05191
9-30-0-2			1.5	4	.026	.031	---	.0394
9-30-0-3			2.6	6	.016	.023	---	.02982
9-30-0-4	30		---	2	---	---	---	---
9-30-0-5			---	4	---	---	---	---
10-1-0-1			4.0	6	.057	.074	---	.07294
10-1-0-2	60		1.6	2	.022	---	---	.2438
10-1-0-3			3.6	4	.125	.180	---	.1573
10-1-0-4			5.5	6	.092	.152	---	.1262
10-2-5-1	10	2.21	1.00	2	.03	.065	---	.04857
10-2-5-2			2.65	4	.023	.040	---	---
10-2-5-3			3.60	6	.020	.034	---	.02536
10-2-4-1	30		1.8	2	.117	---	---	---
10-2-4-2			3.7	4	.08	.13	---	---
10-2-4-3			4.75	6	---	---	---	---
10-2-3-1	60		1.9	2	.188	---	---	.02246
10-2-3-2			4.0	4	.161	---	---	---
10-2-3-3			5.0	6	.137	---	---	.1343

TABLE C.4 (con't)

Film #	L(cm)	d(cm)	ΔP(psid)	P(psig)	t_1 (sec)	t_2 (sec)	t_3 (sec)	t_4 (sec)
9-22-0-1	30	4.7	2.0	3	.060	---	---	.1039
9-22-0-2			3.25	4	.052	---	---	---
9-22-0-3			4.07	5	.045	---	---	.07204
9-22-0-4			---	7	.040	---	---	---
9-23-1-1	20	4.7	1.275	2	.089	---	---	---
9-23-1-2			2.15	3	.079	---	---	---
9-23-1-3			2.875	4	.071	---	---	---
9-23-1-4			3.25	5	.064	---	---	---
9-2 -1-5				6	.058	---	---	---
9-23-2-1	10	4.7	1.125	2	.032	.039	---	.04558
9-23-2-2			1.625	3	.025	.032	---	---
9-23-2-3			1.925	4	.022	.029	---	---
9-23-2-4			2.175	5	.021	.027	---	.03299
no film	45	4.7	---	2	---	---	.165	---
			---	3	---	---	.110	---
			---	4	---	---	.094	---
			---	5	---	---	.084	---
			---	6	---	---	.080	---
no film	30	4.7	---	2	---	---	.104	---
			---	3	---	---	.07	---
			---	4	---	---	.06	---
			---	5	---	---	.056	---
			---	6	---	---	.05	---
9-3-2-2	60	4.7	---	2	.582	---	---	---
9-3-2-3			---	5	.127	.193	---	---
9-3-2-4			---	8	.098	.139	---	---

731 126

TABLE C.5   Maximum Swell Height Data for 46 mm Diameter Tube

Submergence Depth cm	Mean Air Velocity cm/sec	Maximum Swell Height, cm									Average Swell Height h cm	$\frac{h}{d}$
		(i)	(ii)	(iii)	(iv)	(v)	(vi)	(vii)	(viii)	(ix)		
8.8	78.0	7.88	6.04	5.51	5.51	6.56	8.14				6.6	1.43
	70.0	7.38	5.54	6.06	6.85	6.06	6.85				6.3	1.37
	62.5	5.22	6.33	5.43	6.06	9.22					6.5	1.41
	54.5	7.11	6.06	5.01	6.6						6.2	1.35
	47	5.01	5.54	6.60	5.80	6.6					5.9	1.28
	39.0	5.8	5.00	4.38	5.0	5.0	4.48				5.0	1.09
	31.0	6.06	3.96	5.27	4.38	5.8	6.06				5.3	1.15
	23.5	3.59	4.22								3.9	0.85
	15.5	3.27	2.90	3.22	3.17						3.1	0.67
27	78.0	4.54	6.59	8.39	6.85	5.06	5.0	7.9	6.1	6.8	6.35	1.38
	62.4	5.3	5.57	5.57	6.34	7.88	5.31	4.8	5.83	4.80	5.71	1.24
	47.0	6.08	5.30	5.00	5.47	6.60	5.57	4.80			5.54	1.20
	31.0	4.54	3.75	3.78	4.8	5.57	5.83	5.00			4.0	0.87
	15.5	4.55	5.31	4.13	4.55	4 03	3.26	3.93			4.25	0.92
18.7	78.0	5.07	5.07	7.39	5.07	7.39	5.75				5.96	1.30
	62.5	4.65	5.43	4.14	4.40	7.50	4.14				5.05	1.10
	47.0	4.14	4.14	5.17							4.48	0.97

TABLE C.5 Maximum Swell Height Data for 46 mm Diameter Tube (continued)

Submergence Depth cm	Mean Air Velocity cm/sec	Maximum Swell Height, cm									Average Swell Height h cm	$\frac{h}{d}$
		(i)	(ii)	(iii)	(iv)	(v)	(vi)	(vii)	(viii)	(ix)		
45	247	12.7	15.2	14.0							14.0	3.0
	209	15.2	14.0	15.2							14.8	3.2
	160	10.2	12.7	9.7							10.9	2.3
30	236	12.7	12.7	15.2	15.2						14.0	3.0
	190	12.7	10.2								11.0	2.4
	190	12.7									12.7	2.8
	152	10.2	7.6	10.2	7.6						8.9	1.9
	114	9.0	7.6	10.2	9.0						8.9	1.9
15	251	10.2	12.7	17.8							13.5	2.9
	205	15.2	12.7	17.8							13.5	2.9
	145	12.7	10.2	12.7							11.9	2.6
	114	11.4	10.2	11.4	12.7						11.4	2.5

53

731 128

Table C.6 Maximum Swell Height Data for 34 mm Diameter Tube

Submergence Depth cm	Mean Air Velocity cm/sec	Maximum Swell Height, cm (i)	(ii)	(iii)	(iv)	(v)	(vi)	Average Swell Height h cm	$\frac{h}{d}$
7	175	9.25	7.00	8.50	7.75	7.50		7.9	2.32
	150	6.25	8.12	8.87	7.37			7.7	2.25
	126	6.62	6.62	7.00				6.8	1.99
	100	6.25	5.50	6.00	5.12			5.7	1.68
	75	5.87	7.34	4.38	6.25	5.87		6.0	1.75
41.5	170	8.6	7.0	9.0	7.4			8.0	2.35
	126	6.7	4.3	7.5	6.7			6.3	1.85
	75	3.9	4.1	4.3	5.7			4.5	1.32
	50	7.1	3.1	5.5	5.5			5.3	1.56
	25	4.7	4.3	3.9				4.3	1.26
65.6	176	6.6	5.3	9.6	6.9	6.4	7.4	7.0	2.07
	126	5.4	7.9	8.4	6.9	6.9	6.9	7.1	2.08
	100	4.46	6.11	5.70				5.4	1.59

Table C.6 Maximum Swell Height Data for 34 mm Diameter Tube (continued)

Submergence Depth cm	Mean Air Velocity cm/sec	Maximum Swell Height, cm							Average Swell Height h cm	$\frac{h}{d}$
		(i)	(ii)	(iii)	(iv)	(v)	(vi)	(vii)		
45	451	17.8	10.2						14.0	4.1
	364	12.7	10.2	10.2					11.0	3.2
30	538	15.2	15.2	17.8	12.7				15.2	4.5
	436	15.2	8.9	10.2	7.6	12.7	10.2	15.2	11.4	3.4
	291	12.7	9.7	10.2	12.7	7.6	12.7		12.7	3.7
	218	8.9	10.2	5.08	10.2				8.6	2.5
	582	15.2	8.9	12.7	15.2	14.0	12.7	12.7	13.1	3.9
	436	12.7	12.7	12.7	12.7		12.7		12.7	3.7
	291	12.7	12.7	11.4	15.2				13.0	3.8

Table C.7 Maximum Swell Height Data for 34 mm Diameter Tube

Submergence Depth cm	Mean Air Velocity cm/sec	Maximum Swell Height, cm						Average Swell Height h cm	$\frac{h}{d}$
		(i)	(ii)	(iii)	(iv)	(v)	(vi)		
66	476	8.75	7.73	8.30				8.30	3.77
	335	6.4	6.4	6.58				6.46	2.94
	230	6.71	7.14	8.4	7.9			7.53	3.42
	123	6.83	7.27	7.02				7.03	3.20
	53	4.90	5.15	4.96				5.00	2.27
40	494	6.22	6.10	6.26				6.16	2.80
	352	6.47	6.47	8.04				6.29	2.86
	211	7.0	7.41	7.41				7.28	3.31
	141	4.92	4.92	5.10				5.00	2.27
6	494	9.15	9.54	9.15	7.6			8.86	4.03
	352	7.6	8.0	10.7	7.23	8.38		8.38	3.81
	211	8.77	8.00	6.46	8.00	7.61		7.77	3.53
	141	5.31	6.46	4.54	5.46	4.92		5.54	2.52
	70	3.19	3.00	4.92	3.77	4.54	5.69	4.18	1.90

Table C.7 Maximum Swell Height Data for 34 mm Diameter Tube (continued)

Submergence Depth cm	Mean Air Velocity cm/sec	Maximum Swell Height, cm						Average Swell Height h cm	$\frac{h}{d}$
		(i)	(ii)	(iii)	(iv)	(v)	(vi)		
60	567	8.9	11.4	6.4	14.0			10. .	4.6
	502	8.9	6.4	7.6	7.6			7.6	3.5
	456	7.6	8.9					7.6	3.5
30	530	20.3	12.7	17.8				17.0	7.7
	446	10.2	10.2	14.0				9.7	4.4
	335	12.7	7.6					10.2	4.6
	242	7.6	5.1					6.4	2.9
10	688	12.7	15.2	16.5				14.8	6.7
	642	10.2	12.7	17.8	10.2			12.7	5.8
	632	17.8	2.54					10.2	4.6
	614	10.2	15.2	14.0	15.3			13.7	6.2
	577	10.2	12.7	15.2	20.3	14.0	15.2	14.6	6.6
	428	15.2	17.8	16.5				12.4	5.6
	260	7.6	7.6	8.9	12.7			9.2	4.2

APPENDIX D

POOL FREE SURFACE RESPONSE DURING STEADY STATE AIR INJECTION

In the case of an actual BWR system, the pool surface swell is caused by the motion of a large bubble, which is continuously fed by the air from the vent pipe. A series of steady state low flow rate experiments were conducted in order to study the swelling behaviour. The flow rate in this set of steady state experiment was maintained at a value 20 to 30 times lower than the maximum value during transient tests. Hence, caution should be applied with the interpretation of these data. Nevertheless, these tests represent our effort to understand the swelling phenomena.

Visual Observations

The motion pictures of the behaviour of the pool free surface during steady state air injection showed, that a crest would form at the free surface, reach a maximum height, fall back and reform at another location and then repeat the cycle. A photograph of the free surface is shown in Figure D.1 when air at cm/sec was injected through 34 mm diameter tube. The cyclic appearance of the crests as observed from the motion pictures is shown in Figures D.2 and D.3 for air velocities of 538 cm/sec and 218 cm/sec. In the experiments conducted up to now, no clear dependence of the distance between location of occurence of consecutive crests on the tube diameter and the flow velocity was discerned. The distance between location of these peaks was found to vary between 6-12 cm. The frequency of swelling of the free surface was noted to be slightly dependent on the flow velocity and was generally observed to be about 4 hertz when the air flow velocity through 34 mm diameter tube was 538 cm/sec. At this point in time, the data are too few to suggest any theoretical explanation for the growth rate and the oscillatory modes of the free surface.
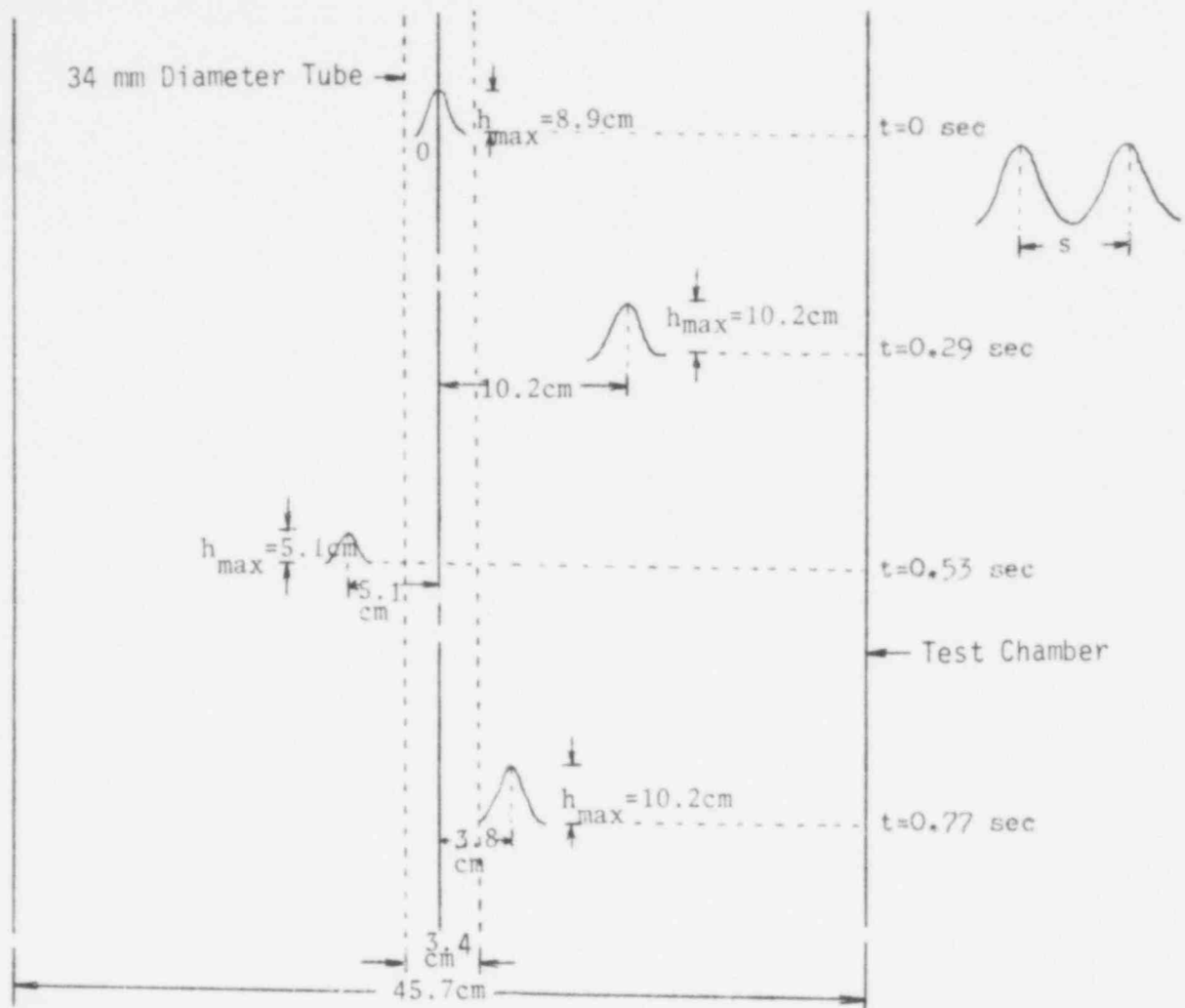
58

Figure D.1   Photograph of Pool Swell Phenomena

59

731 134

Fig. D.2   Pool Free Surface Behavior during Injection of Air at
           538 cm/sec through 34 mm Diameter Tube.
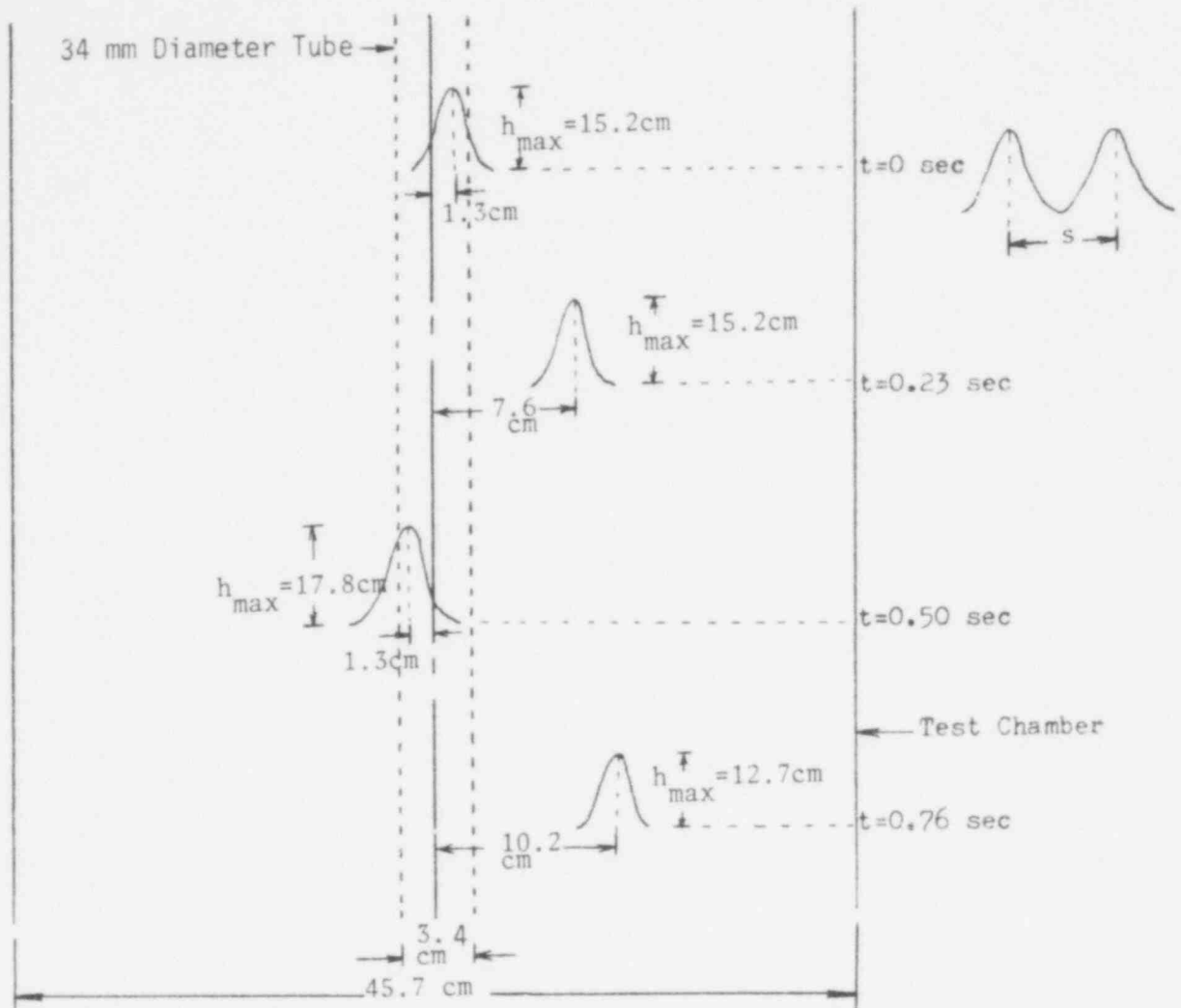
a) $(h_{max})_{ave} = \dfrac{15.2 + 15.2 + 17.8 + 12.7}{4} = 15.2$ cm

b) $(s)_{ave} = \dfrac{6.3 + 8.9 + 11.5}{3} = 8.9$ cm

c) Frenquency of Appearance of a Crest = 4 / sec

731   135

a) $(h_{max})_{ave} = \dfrac{8.9 + 10.2 + 5.1 + 10.2}{4} = 8.6cm$

b) $(s)_{ave} = \dfrac{10.2 + 15.2 + 8.9}{3} = 11.4cm$

c) Frenquency of Appearance of a Crest = 3.88 / sec

Figure D.3 Pool Free Surface Behavior during Injection of Air at
218 cm/sec through 34 mm Diameter Tube.

731 136

Maximum Swell Height Data

The maximum pool swell height data for tubes of 46 mm, 34 mm and 22 mm diameter was obtained by varying the air flow velocity and the submergence depth of the tubes. These data are presented in Appendix C. The maximum free surface height is seen to be strongly dependent on the tube diameter and the flow velocity, but is independent of the submergence depth. The maximum swell height when non-dimensionalised with the tube diameter is found to correlate with Froude number defined as

$$Fr = \frac{\rho_a U_a^{\,2}}{\rho_w \, g \, d} \tag{4.8}$$

The maximum swell height data for 46 mm diameter tube is plotted as a function of Froude number in Figure D.4. The data for Froude number varying from 1.5×10^{-4} to 2×10^{-2} are seen to be correlated well with the relationship

$$\frac{h}{d} = 10.3 \left(\frac{\rho_a U_a^{\,2}}{\rho_w g d} \right)^{0.3} \tag{4.9}$$

Figure D.5 shows the swell height data for 34 mm diameter tube. The data for Froude number varying from 4×10^{-4} to 6×10^{-2} are again correlated fairly well by equation (4.9). The swell height data for 22 mm diameter tube are plotted in Figure D.6 For small Froude numbers, the data lie higher than predicted by equation (4.7). But, for higher flow velocites data tend to follow the relationship of equation (4.9). This trend of the data indicate that at higher flow velocities or for larger tube diameters the interference effects of the test chamber wall are dominant. However as the tube diameter is decreased in relation to the test chamber diameter, the fluid surrounding the tube start to behave as an infinite medium. The effect of tube diameter on swell height is demonstrated more clearly in Figure D.7.
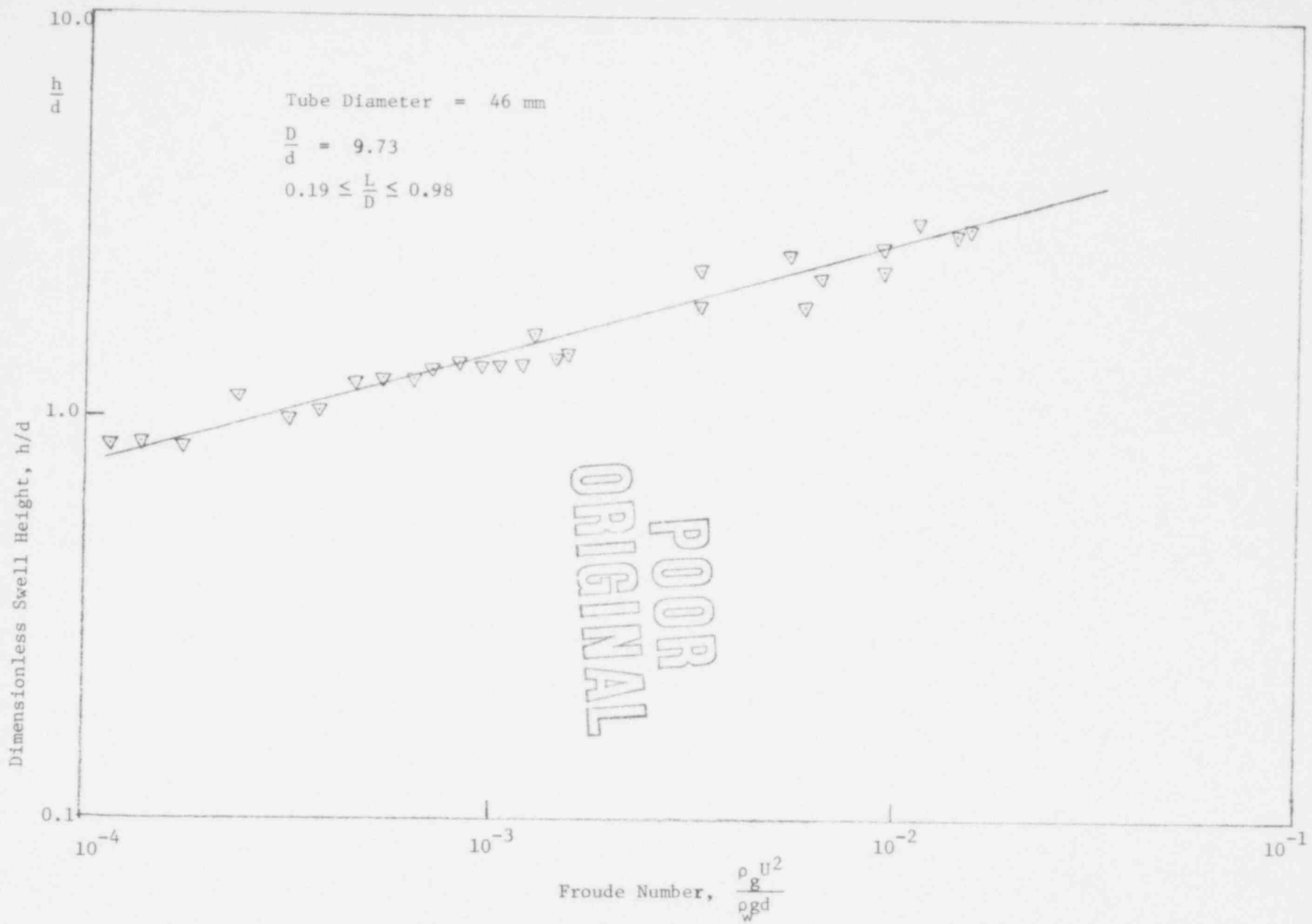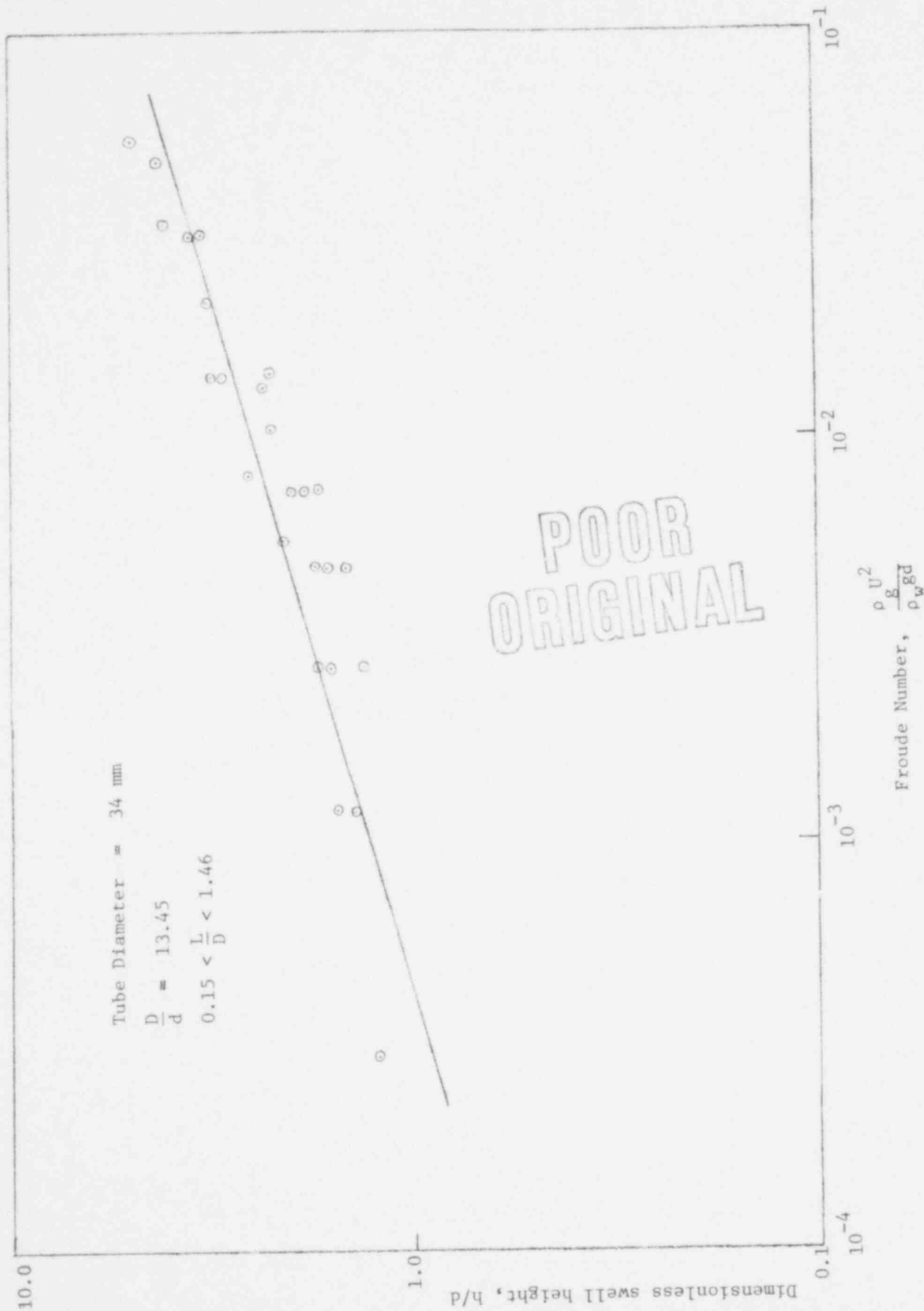
731 137

Figure D.4   Swell Height as a Function of Froude Number for 4.60 cm diameter tube

Figure D.5   Swell Height as a Function of Froude Number for 3.4 cm diameter tube

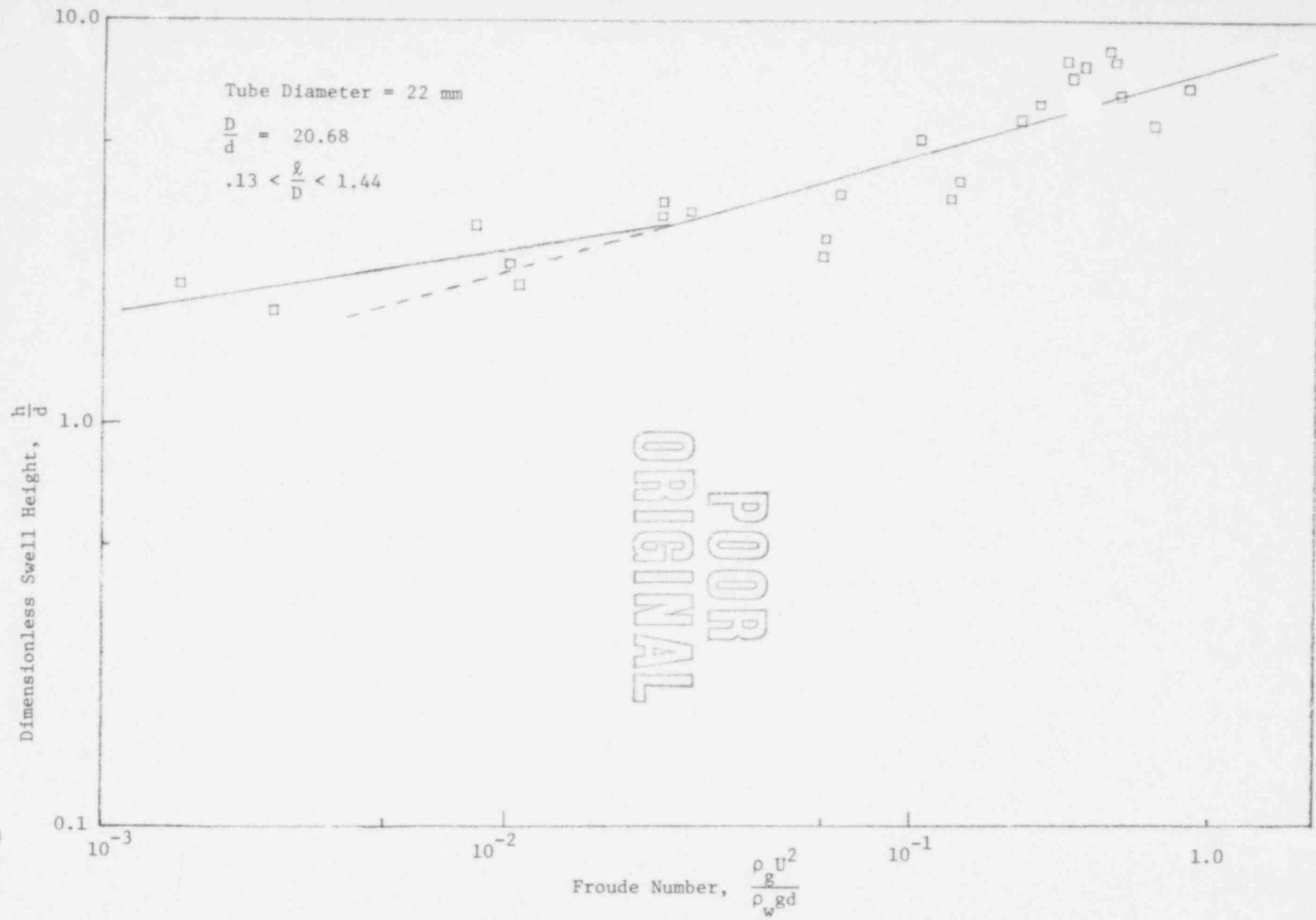Tube Diameter = 34 mm

$\frac{D}{d} = 13.45$

$0.15 < \frac{L}{D} < 1.46$

Froude Number, $\frac{\rho}{\rho_w} \frac{U^2}{gd}$

Dimensionless swell height, h/d

POOR
ORIGINAL

64

731 139

Figure D.6   Swell Height as a Function of Froude Number for 2.2 cm diameter tube

Finally, all the swell height data contained in Figures D.4, D.5 and D.6 are plotted in Figure D.8. The dimensionless swell height is seen to be correlated well by the relationship.

$$\frac{h}{d} = 10.3 \; [Fr^{0.3}] + 4.5 \; \exp \; [- 1.30 \times 10^3 \; (\frac{d}{D})^2 \; (Fr)^{1/12}] \qquad (4.10)$$

731 141
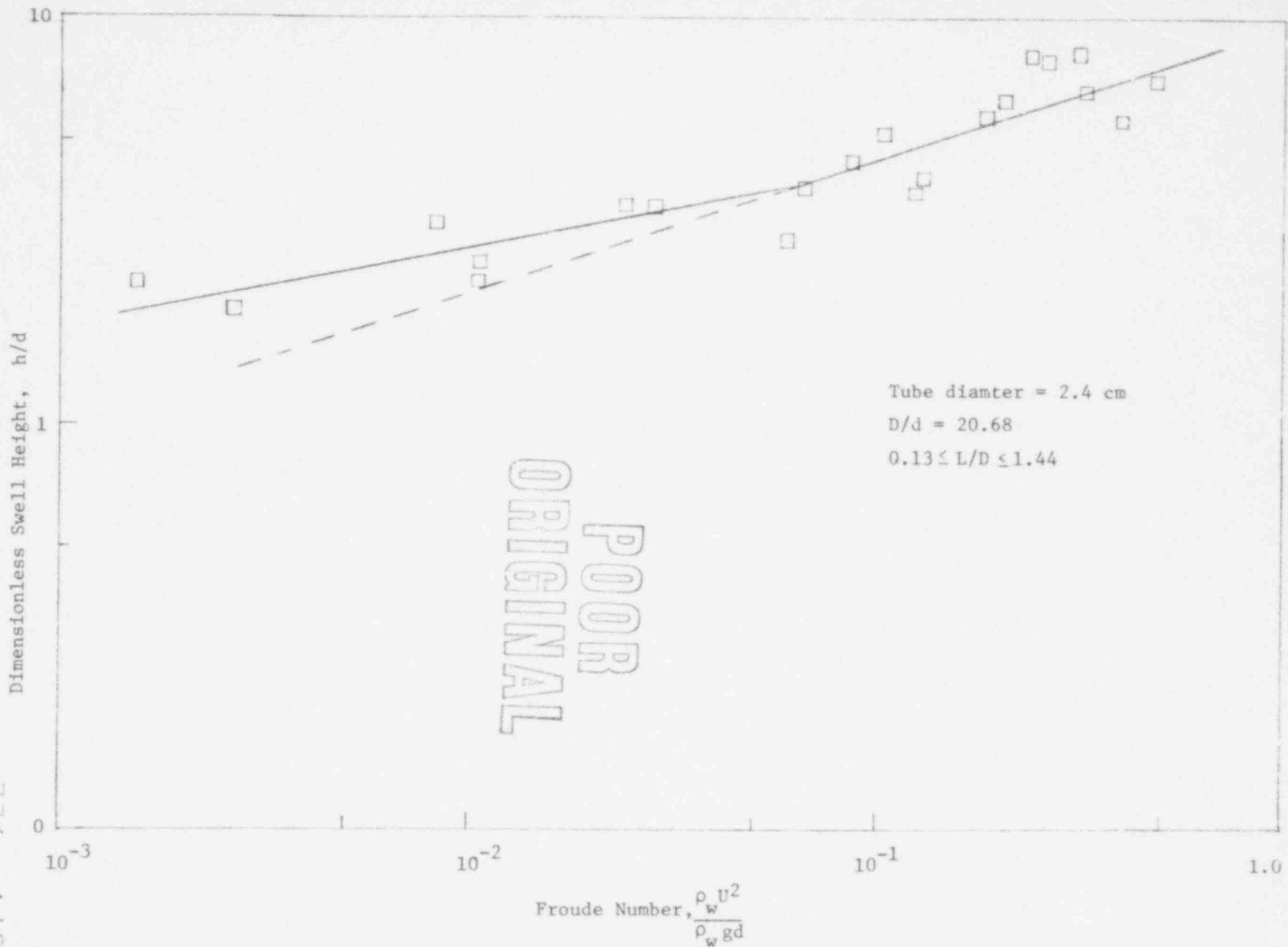
Figure D.6   Swell Height as a Function of Froude Number for 2.40 cm diameter tube
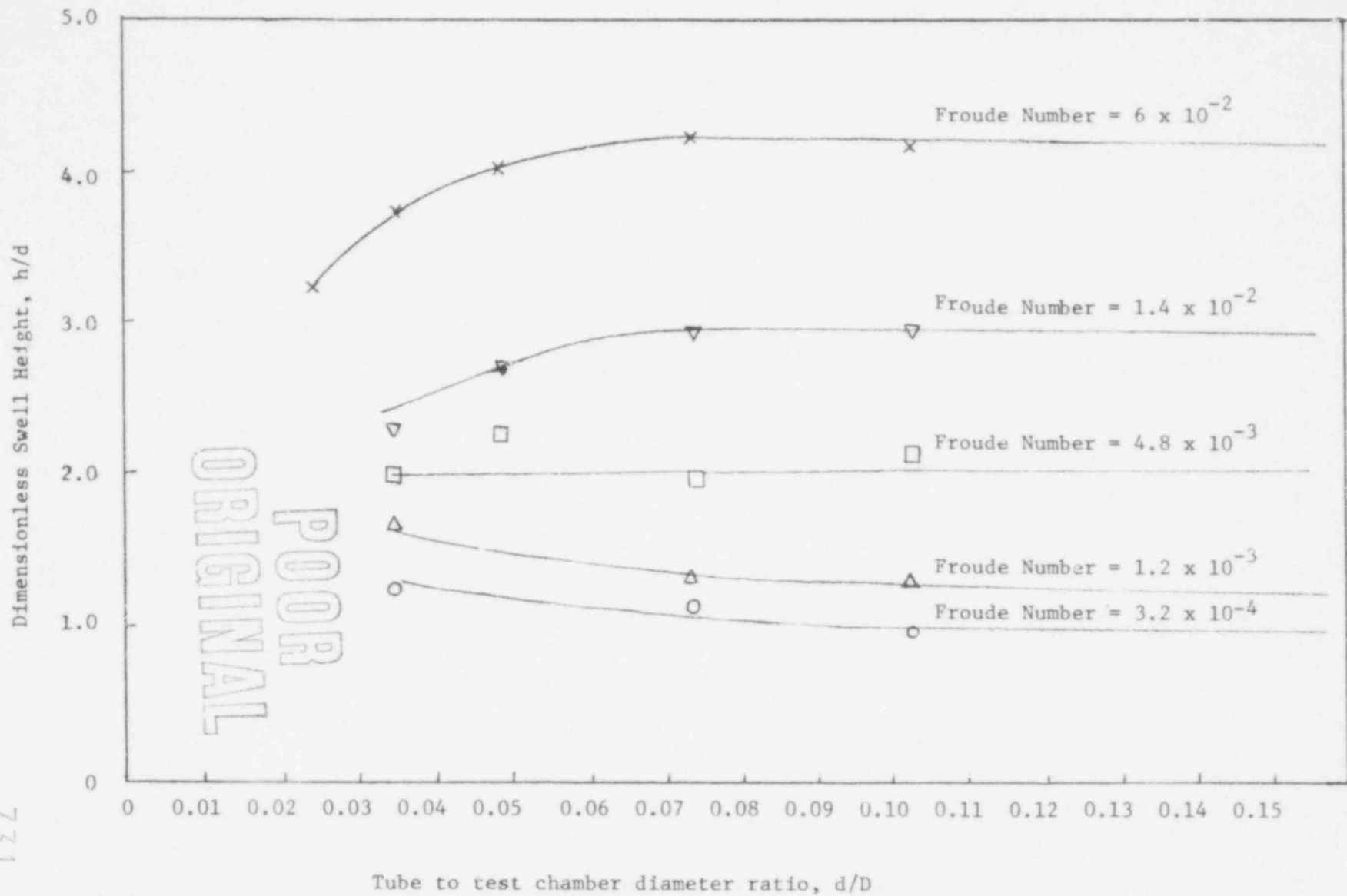
Figure D.7   Effect of Ratio of Tube to Test Chamber diameter on Swell Height
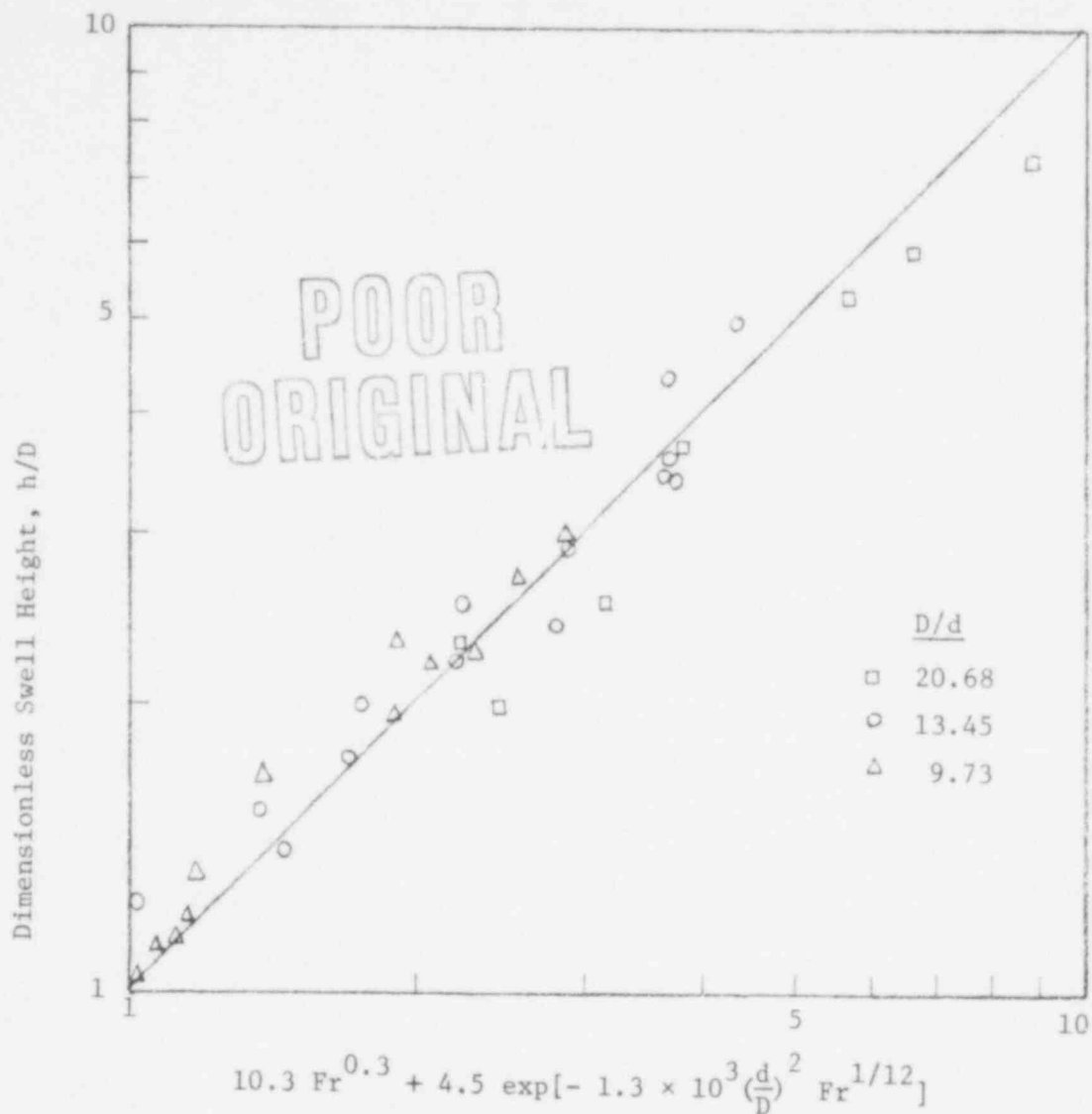
Figure D.8   A General Correlation for Swell Height····

731 145